# Does Earthquake Stress Drop Increase with Depth in the Crust?

Abercrombie, R. E.[1*], D. T. Trugman[2], P. M. Shearer[3], X. Chen[4], J. Zhang[4], C. N. Pennington[4,5], J. L. Hardebeck[5], T. H. W. Goebel[6] and C. J. Ruhl[7]

1. Department of Earth and Environment, Boston University, Boston USA
2. Jackson School of Geosciences, University of Texas at Austin
3. Scripps Institution of Oceanography, University of California San Diego, La Jolla, CA
4. School of Geosciences, the University of Oklahoma, Norman, OK
5. USGS, Moffett Field, California
6. Center for Earthquake Research and Information, University of Memphis, 3890 Central Ave, Memphis, TN 38152
7. Department of Geosciences, The University of Tulsa, Tulsa, Oklahoma

* corresponding author rea@bu.edu

*Revised for Submission to Journal of Geophysical Research – Solid Earth*
*July 2021*

Key Points:

- A stacked spectral ratio approach can separate depth dependence of source and path effects
- Analyses of spectral decomposition inversions suggest that previous reports of increase in stress drop with depth may be overstated
- Source parameter analyses should explicitly include depth-dependent attenuation models or empirical corrections.

## *1* Abstract:

We combine earthquake spectra from multiple studies to investigate whether the increase in stress drop with depth often observed in the crust is real, or an artifact of decreasing attenuation (increasing $Q$) with depth. In many studies, empirical path and attenuation corrections are assumed to be independent of the earthquake source depth. We test this assumption by investigating whether a realistic increase in $Q$ with depth (as is widely observed) could remove some of the observed apparent increase in stress drop with depth.

We combine event spectra, previously obtained using spectral decomposition methods, for over 50,000 earthquakes (M0 to M5) from 12 studies in California, Nevada, Kansas and Oklahoma. We find that the relative high-frequency content of the spectra systematically increases with increasing earthquake depth, at all magnitudes. By analyzing spectral ratios between large and small events as a function of source depth, we explore the relative importance of source and attenuation contributions to this observed depth dependence.

Without any correction for depth-dependent attenuation, we find a systematic increase in stress drop, rupture velocity, or both, with depth, as previously observed. When we add an empirical, depth-dependent attenuation correction, the depth dependence of stress drop systematically decreases, often becoming negligible. The largest corrections are observed in regions with the largest seismic velocity increase with depth. We conclude that source parameter analyses, whether in the frequency or time domains, should not assume path terms are independent of source depth, and should more explicitly consider the effects of depth-dependent attenuation.

## *2* Plain Language Summary:

The stress release (or stress drop) during an earthquake provides information about the energy budget, and the slip and area of rupture, which are needed to investigate earthquake triggering and rupture dynamics. Stress drop is also an important element of seismic hazard forecasting since high stress drop earthquakes radiate more high frequency energy, resulting in stronger ground shaking. As depth increases in the earth, the stress on faults increases because of the increased weight of the rocks above. Therefore, many models predict that deeper earthquakes should have higher stress drops. Deeper earthquakes radiate more high frequency energy than shallow ones, and some studies have interpreted this as an increase in stress drop with depth. However, attenuation of seismic energy as the waves travel through the earth is also depth-dependent, and this is rarely explicitly included in analyses. We perform a combined analysis of frequency spectra from over 50,000 previously studied earthquakes. We compare ratios of large to small magnitude earthquakes, from different depth ranges, to separate the effects of depth-dependent source radiation from depth-dependent attenuation. We find that depth-dependent attenuation can have a first-order effect and account for much of the previously reported apparent increase in stress drop with depth.

## 3 Introduction

The stress release, or stress drop, during earthquake rupture has long been thought to be directly related to the magnitude of the ambient stress (e.g., Byerlee & Brace, 1968; Sibson 1974; Scuderi *et al*., 2016). For example, in a rate-and-state frictional model of earthquake rupture, stress drop is a function of the normal stress, and also any changes in frictional effects with slip velocity (e.g., Dieterich, 1979; Marone, 1998). The normal stress dependence is of particular interest because it implies that earthquake stress drop should increase linearly with depth throughout the seismogenic crust, and so is quantifiable (e.g., Sibson, 1974; Zoback & Harjes, 1997). Determining whether earthquake stress drop really increases with depth in the crust is hard because of the large uncertainties in stress drop measurements; some studies have reported an increase (e.g., Hardebeck & Aron, 2009; Boyd *et al*., 2017; Huang *et al*., 2017; Trugman, 2020) and others have not (e.g., Shearer *et al*., 2006; Allmann & Shearer 2007). The depth dependence of the source radiation also has implications for seismic hazard; Parker *et al*. (2020) found that the intensity-based stress drops and peak ground accelerations of the deeper aftershocks of the 2019 Ridgecrest earthquake are underpredicted by existing ground motion equations.

Seismic moment is proportional to slip multiplied by the area of rupture, and so combining measured seismic moment with an estimate of the rupture dimension (and hence area) allows calculation of the slip, and thus the strain and stress release. To resolve spatial and depth variation of source parameters within the crust, we must use the more numerous smaller earthquakes (<M4 or M5). For these earthquakes, source dimension is estimated from the source duration (e.g., Mori *et al*., 2003), or by modeling the spectral shape (e.g., Brune, 1970) and so assumptions of both geometry (typically circular) and rupture velocity (typically constant or linearly increasing with depth) are required for stress drop calculations (e.g., Kaneko & Shearer, 2015).

As seismic velocities increase with depth in the earth, it seems reasonable that the rupture velocity would do the same, perhaps as a relatively constant fraction of the shear wave velocity. Marty *et al*. (2019) found both the release in stress and the rupture velocity to increase with confining stress in laboratory models. Studies of stress drop as a function of depth usually investigate whether reasonable increases in rupture velocity with depth are sufficient to explain

any apparent trend; for example, Shearer *et al*. (2006) and Allmann and Shearer (2007) found that the expected rupture velocity increase was sufficient to compensate for any apparent increase in stress drop, whereas Huang *et al*. (2017), Boyd *et al*. (2017) and Hardebeck and Aron (2009) found the increase in stress drop they observed to be too large to be an artifact of increasing rupture velocity.

Unfortunately, both the rupture dimension and stress drop of small earthquakes are very hard to measure, largely because of the difficulty of removing the effects of propagation through the earth from the recorded seismograms (see Abercrombie, 2021 for a review). The attenuation structure of the earth is not sufficiently well known at the relatively high frequencies needed to resolve small earthquake source parameters, and so empirical Green's function (EGF) approaches have become popular for isolating the source radiation (e.g., Mori & Frankel, 1990; Abercrombie *et al*., 2017; Ross *et al*., 2017). Source parameters obtained in this way are thought to be the most reliable, but they can still be subject to large uncertainties and trade-offs due to the limited frequency range of the signal, as well as the simplifying model assumptions (e.g., Abercrombie 2015; Yoshimitsu *et al*., 2019; Shearer *et al*, 2019; Abercrombie, 2021). These problems affect both time and frequency domain analyses, and the availability of an appropriate EGF event also severely limits the number of earthquakes that can be analyzed in this manner.

Prieto *et al*. (2004) and Shearer *et al*. (2006) introduced the spectral decomposition approach as a relatively data-driven, model-independent method of obtaining consistent source parameter measurements for large numbers of small earthquakes. This approach has since been used in many other studies, with various adaptations and variations, to look for spatial and temporal variation in earthquake source parameters (e.g., Hardebeck & Aron, 2009; Chen & Shearer, 2011; Trugman & Shearer, 2017; Trugman, 2020). The underlying separation of source, path and site effects is similar to that in other generalized inversion schemes (e.g., Oth *et al*., 2011; Bindi *et al*., 2020a), but they differ in how they remove site effects that are common to all stations. Shearer *et al*. (2019) demonstrated how trade-offs between parameters remain a serious problem in large scale inversion studies, because of the limited frequency bandwidth available. They also concluded that relative parameters were better resolved than absolute values, a finding supported by the comparative analysis of Pennington *et al.* (2021).

The spectral decomposition and generalized inversion approaches are powerful as they use recordings from large numbers of earthquakes and stations to increase stability, but in doing so

significant simplifications are required to constrain the number of unknown parameters. The parametrization of attenuation and estimation of site effects used in these approaches implicitly assume that the attenuation experienced depends only on the travel time from source to receiver, and is independent of the source depth of each earthquake. Complementary inversions, that make simplifying assumptions about the source to focus on the attenuation structure (e.g., Hauksson & Shearer, 2006; Eberhart-Phillips, 2016), often find that $Q$ increases, and attenuation strongly decreases, with depth, as observed in deep boreholes (e.g., Abercrombie, 1997). These results are consistent with earlier work by Hough and Anderson (1988) that showed significant depth variation of $Q$ in the crust. If $Q$ increases significantly with depth, then the attenuation experienced by waves from a deeper earthquake could be significantly less than that experienced by waves from a shallower earthquake over the same length of travel time (apart from localized site effects). Ignoring this could potentially lead to a depth-dependence in attenuation being interpreted as a depth dependence in stress drop.

A few studies have investigated explicitly including depth-dependent attenuation in the inversions (e.g., Edwards 2008, 2009), finding that it can compensate for the depth increase in stress drop which results from assuming attenuation is independent of source depth. Most studies have preferred a simpler parametrization where attenuation depends only on travel time, to minimize the number of free parameters in the inversion (e.g., Shearer *et al*., 2006; Bindi *et al*., 2020a). Goertz-Allmann and Edwards (2014) compared the two approaches, and found that they needed to include frequency-dependent $Q$ to obtain agreement, under the assumption of attenuation independent of earthquake source depth. Including depth-dependent attenuation in the inversion was able to compensate for the depth increase in stress drop observed without it. However, they did not investigate the effects of explicitly including depth-dependent $Q$ in the spectral decomposition approach.

Here we compile event spectra from previous studies and analyze them systematically to investigate whether we can distinguish between depth-dependent source and path effects. Our goal is to determine whether previously reported increases in stress drop with depth could be an artifact of failing to correct fully for depth-dependent $Q$. We do not attempt to calculate absolute stress drop estimates in all the different regions. We begin by describing the event spectra that form the basis of our analysis, and the velocity models that we use. We then relate our investigation of the depth dependence of spectral shape, and how we use spectral ratios between

different sets of earthquakes in specific magnitude and depth ranges to distinguish between source and path effects. We find that a significant amount of previously reported increase in stress drop with depth is an artifact of assuming no change in attenuation with depth.

# 4 Event Spectra from Previous Spectral Decomposition Analysis

## 4.1 Theoretical Background to Calculation of Event Spectra

We analyze the event spectra calculated following the general spectral decomposition method introduced by Prieto *et al*. (2004) and Shearer *et al*. (2006) in the 12 studies listed in Table 1. The event spectra obtained by this method are essentially the relative source spectra, averaged over all stations, after correcting for path and site terms. At each available station, the amplitude spectrum of a time window of approximately 1s (depends on the study) containing the direct P wave from an earthquake is calculated and compared to a similar spectrum of a preceding noise window. If the signal is larger than the noise by some threshold in the required frequency range, then the spectrum is included in the decomposition analysis. Details of the precise parameter values and thresholds are given in the original studies.

The aim of spectral decomposition is to isolate the contributions of the source, path and site effects in the recorded spectra, taking advantage of the fact that stacking (or averaging) large numbers of spectra will compensate for uncertainties from irregularities in individual observations. Each spectrum ($X_{ij}(f)$) from source *i*, recorded at station *j* can be considered a product of the source, path and site effects:

$$X_{ij}(f) = e_i(f) \times s_j(f) \times t_{k(i,j)}(f) \times r_{ij} \qquad (1)$$

where the site effect at a station ($s_j(f)$) is common to all events, $t_{k(i,j)}(f)$ is the travel-time dependent path effect over path *k*, the event term ($e_i(f)$) includes the source and any site or local path effects common to all stations, and $r_{ij}$ is the residual. The travel time term ($t_{k(i,j)}(f)$) is typically discretized into 1 s increments of travel time. Equation 1 is typically solved using a robust least-squares approach that varies by study, iteratively solving for $s_j(f)$, $t_{k(i,j)}(f)$,and $e_i(f)$, minimizing $r_{ij}$.

To solve equation (1), the general spectral decomposition method assumes no source directivity, or focal mechanism corrections, and that the available stations provide a reliable

192 average of the focal sphere (e.g., Kaneko & Shearer, 2015). At this stage in the analysis, there is
193 no assumed spectral shape or model for any of the terms, such as a Brune source model (Brune,
194 1970), or exponential attenuation (e.g., Anderson and Hough, 1984). In all implementations of
195 the spectral decomposition approach considered here, it is also assumed that $t_{k(i,j)}$ depends only
196 on the source-receiver travel time, and is otherwise independent of the location or depth of the
197 earthquakes; no lateral or azimuthal variations in attenuation within the study volume are
198 considered. The calculation of independent attenuation functions for different travel-time lengths
199 allows for differences in attenuation for longer ray paths that on average are deeper, and hence
200 the attenuation per unit travel time is typically less for the longer travel-times (see Trugman,
201 2020, Supplementary Figure S6, for example). This is consistent with the pattern of attenuation
202 observed in structures in which $Q$ increases with depth (e.g., see Figure 9a of Eberhart-Phillips,
203 2016). For recordings within only a few times the source depth, paths of the same travel time can
204 be very different for deeper and shallower earthquakes. The travel-time term also contains the
205 effects of geometrical spreading which can be distance dependent.
206 To extract the earthquake source spectra from the event spectra ($e_i(f)$), a further
207 correction is needed to separate out any site and local path effects that are common to all
208 stations. In studies following the approach of Shearer *et al*. (2006), this is accomplished using a
209 global EGF or empirical correction spectrum (ECS), typically based on the assumption that the
210 source spectrum matches the Brune source model. Other approaches (e.g., Bindi *et al*., 2020a;
211 Oth *et al*. 2011) select reference sites at which they assume there is no frequency dependent site
212 response.
213 To avoid the inherent ambiguity and uncertainty in available approaches for site response
214 correction, we design an analysis procedure that uses only relative parameters. In this way, site
215 effects common to all events effectively cancel out and do not influence our results. Here, we
216 analyze ratios of the event spectra of pairs of earthquakes that are the direct result of spectral
217 decomposition following equation 1, without applying any assumed or empirical corrections. We
218 cannot obtain absolute parameter estimates, but we can isolate the causes of relative variation.
219 Each event spectrum represents an average for the earthquake over available stations at
220 varying distances, after removal of the site and travel-time dependent terms. It is impossible to
221 invert or model these event terms for any quantities that depend on travel time because there is
222 no single travel time applicable to an event spectrum. Inverting for depth dependent attenuation

would involve going back to the original recorded spectra and performing a new type of inversion allowing for more variation in the travel-time terms, and consequently increased free parameters, trade-offs and uncertainties. One aim of the work presented here is to determine whether such an inversion may be required in future studies, and to find the balance between potential bias from over-simplification and the lack of constraints for greater numbers of free inversion parameters.

## 4.2 Data

We reanalyze the event spectra obtained from 18 separate spectral decomposition inversions in 12 analyses of P-wave spectra listed in Table 1. These include regions of northern California, southern California, Nevada, Oklahoma and Kansas, and include both natural tectonic and induced seismicity (Figure 1). Table 1 also shows the varying numbers of events, their magnitude and depth ranges, and signal frequency ranges available for each individual study. Most analyses used surface recordings from regional seismic networks (typically 100 samples/s data) and temporary deployments, but the analyses by Hardebeck and Aron (2009) and Zhang *et al*. (2019) on the Hayward Fault and the San Andreas Fault at Parkfield, respectively, used higher frequency shallow borehole network recordings. All analyses followed the same general decomposition process based on equation 1, except for the analysis of Landers aftershocks by Shearer *et al*. (2019). Their analysis of a very dense (6 km) cluster of Landers aftershocks meant that there was so little variation in travel time to each station, the $t_{k(i,j)}(f)$ term could be ignored, and the path attenuation was absorbed by the station terms, $s_j(f)$.

Following Shearer *et al*. (2006) and Chen and Shearer (2011), we only include event spectra calculated from at least 5 stations that meet the signal to noise threshold. As we do not include lateral variation in our analysis, we also subset the events from a number of studies that included distinct populations of earthquakes (Table 1); the precise area polygons are provided in the Supporting Information. Following the depth dependent analysis by Hardebeck and Aron (2009), we only investigate the earthquakes in their study that occurred along the Hayward Fault. We also select two sub-regions from the Bay Area analysis of Trugman and Shearer (2018), based on the SF-CVM regional 3D velocity model (Aagaard *et al*., 2020) to minimize the effects of lateral variations in velocity structure: one including the San Andreas and Hayward Faults, and the second in the Livermore Basin. The study of the Salton Sea region by Chen and Shearer

(2011) included both shallow earthquakes related to geothermal energy production, and parts of the southern San Andreas Fault with a very different hypocentral depth distribution. We select events in these two separate regions, and also limit our analysis to earthquakes since 1989 due to changes at the time in the recording network. Chen and Shearer (2011) applied different empirical corrections to the event spectra for the pre and post 1989 earthquakes in their analysis, but as most earthquakes occurred in the later time period, and we did not want to complicate our analysis with extra corrections, we simply discarded the earlier earthquakes. For all other regions, we used all the earthquakes in the original studies that met the signal to noise criterium. The numbers of earthquakes included from each study, in each sub-region are given in Table 1, and range from 364 to 15671, with a median of just over 2000.

For analysis of source parameters, we require consistent estimates of the earthquake magnitude; we can also use the catalog magnitudes ($M_L$), but they contain significant uncertainties (e.g., Pennington *et al*., 2021). As not all the original calculated values are available, we follow the original studies, to recalculate them. We calculate the relative amplitudes of the low frequency spectra (using the same frequency ranges as the original studies, given in Table 1). For consistency, we assume that at $M_L$=3, $M_W$=$M_L$ for all regions (following Shearer *et al*., 2006), and so convert these relative moments into absolute estimates of seismic moment, and moment magnitude.

## 5 Observations of Depth Dependence to the Shape of Event Spectra

As a first step we investigate whether the frequency content of the event spectra varies consistently with hypocentral depth. All of the earthquakes considered here have been relocated using waveform cross-correlation based methods, either in the original spectral decomposition studies, or earlier, and we use these same published values (see references in Table 1). We then calculate the geometric mean amplitude of each event spectrum in both a low frequency range and a high frequency range, and calculate the ratio between these amplitudes as a measure of the spectral shapes. As the spectral shape also varies with earthquake magnitude, we plot the results in narrow magnitude bins for each region. Figure 2 shows that at all magnitudes, the relative high frequency energy increases with depth for earthquakes in the Ridgecrest sequence (event spectra from Trugman, 2020). This observation is entirely consistent with the increase in stress drop with depth reported by Trugman (2020), although it is also consistent with an increase in rupture

velocity with depth, a decrease in attenuation with depth, or some combination of all three. Another example is shown in the Supporting Information (Figure S1). Figure 3 shows results for a single magnitude bin for all studies and sub-regions, and reveals that a similar increase in relative high frequency energy is observed in the other studies. Again, this result is consistent with the previously reported increase in stress drop with depth. These examples use binning by moment-magnitude (the number of events in each bin are shown in the Supporting Information, Figures S2 and S3), but the results are essentially the same for local magnitude.

These systematic observations of depth dependent spectral shape could be caused by either variation in source radiation (e.g., stress drop, rupture velocity), or in attenuation, or both. Before we attempt to distinguish between these competing effects, we investigate whether there is any relationship between changes in spectral shape and local seismic velocity structure. We plot representative 1D velocity models for each region in Figures 2 and 3. These models are derived from a variety of sources, detailed in Table 1, and are selected to approximate the structure in the volume sampled by all the different ray paths from earthquakes to stations in each region. In some regions, we are able to use specific velocity models derived from local relocations and velocity inversions (e.g., Thurber *et al*., 2006; Toth *et al*., 2012; Chen, 2016; Ruhl *et al*., 2016; Rubinstein *et al*., 2018; Lomax, 2020). For other regions in Southern California we estimate the mean 1D velocity structure by sampling each epicentral region within the Southern California Earthquake Center (SCEC) Community Velocity Model version H15.1 (SCEC CVM-H15.1; Shaw *et al*., 2015) using the SCEC Unified Community Velocity Model (UCVM) software (Small *et al.,* 2017). For the Livermore and Bay Area regions in Northern California, we similarly sample the USGS San Francisco Bay Region 3D (SF-CVM) seismic velocity model (Aagaard *et al*., 2020. Also, in some regions we include two models for comparison, either from similar studies (e.g. in the Salton Sea region) or for both sides of a major fault, as in the case of the Hayward fault (following Hardebeck & Aron, 2009).

A visual comparison of the variation in high frequency content of the event spectra with depth, and the representative velocity structures (Figure 3) suggests that the change in spectral shape is greater where there is greater change in velocity structure; for example, compare the Hayward Fault, Livermore and Parkfield to locations in Southern California. Kansas and Oklahoma exhibit a very rapid increase in velocity at shallow depths, but these correspond to

sedimentary layers that are not sampled by many earthquakes, and so it is hard to see if there is any connection.

# 6 Investigation of Depth Dependent Path Effects Using Spectral Ratios

## 6.1 Hypothesis

The spectral decomposition analysis used to obtain the event spectra implicitly assumes that the along path attenuation is dependent only on the travel time, and so does not depend directly on the depth of the earthquake. If $Q$ does increase with depth, then rays with the same travel time, but from sources at different depth, could experience significantly different attenuation, as illustrated in the cartoon in Figure 4. If this depth dependence is ignored, as in spectral decomposition or analogous, generalized-inversion based approaches, then any variation in attenuation with depth will become part of the event terms, potentially appearing as a variation in stress drop with depth. In this cartoon, and in our synthetic models, we assume that the horizontal distance to the stations is greater than the focal depth, as is true for most stations used in such source parameter analyses.

We devise an empirical Green's function (EGF) approach to test whether variation in attenuation with depth could explain the increase in stress drop with depth reported by a number of spectral decomposition studies. Our approach is illustrated by the cartoons in Figure 4; for each study, we consider a group of earthquakes that are shallow and another that are deep. Then we calculate spectral ratios between large and small earthquakes, assuming that the smaller events in each group serve as empirical Green's functions for the larger ones. We consider the case shown in Figure 4(a) where smaller earthquakes of any depth can be considered EGFs for the larger events of any depth. We compare this geometry to results where we use only smaller events of the same depth range as the larger ones Figure 4(b); i.e., we use only deep small events as EGFs for deep large events, and only shallow small events as EGFs for shallow large events. We refer to this geometry as using depth-specific EGFs to correct for the depth-dependent attenuation.

To demonstrate the possible outcomes, we calculate three simple, synthetic examples in Figure 5. In Figures 4 and 5 we introduce a consistent color scheme that we use throughout the paper to improve clarity. We consider the effects of either (a) attenuation decreasing ($Q$

increasing) with depth, but stress drop remaining constant; (b) attenuation decreasing with depth and stress drop increasing with depth (by a factor of 3 between the two populations); and (c) attenuation constant with depth (as assumed in previous spectral decomposition studies) and stress drop increasing with depth (again by a factor of 3). We calculate synthetic recorded spectra using Equation 2 which combines the simple, circular, Brune source model (Brune, 1970) with exponential attenuation (e.g., Anderson and Hough, 1984).

$$X(f) = \frac{M_0}{1+\left(\frac{f}{f_c}\right)^2} e^{-\pi f t^*} \qquad (2)$$

The synthetic spectrum ($X$) is calculated from the seismic moment ($M_0$) and corner frequency ($f_c$), over frequency ($f$). The attenuation ($t^*$) = $t$ /$Q$ where $t$ is the travel time, and $Q$ is frequency independent for the purposes of clarity. We assume moment magnitude ($M_W$) of 3 and 2, for the large and small earthquakes, respectively, and t = 10 s for all events in this simple example. We assume that the stations are sufficiently distant that ray paths leaving the events travel nearly horizontally, such that the shallow-event rays spend more time in the low-Q layers near the surface than the deeper events (see Figure 4). For the purposes of this synthetic exercise, we simplify and approximate the attenuation difference using fixed t* values for the deep and shallow events. The assumed parameters are given in Table 2. Varying the assumed geometry and parameters of the model will obviously affect the shapes of the calculated spectra. The aim of our synthetic example is simply to demonstrate the pattern of the effects, and show that they can be significant.

In all cases in the top row of Figure 5, we observe that the deeper events have relatively more energy at high frequencies than do the shallow, consistent with the observations in Figures 2 and 3.

The middle row of Figure 5 demonstrates what we would expect to observe using our EGF-based approach for the different scenarios. Without any correction for depth dependent attenuation, there is a clear difference between the spectral ratios obtained for large deep and large shallow earthquakes in all cases (difference between the dark and light red curves, see legend). If attenuation varies with depth, then correcting for this by using depth-specific EGFs (dark and light blue curves) significantly decreases the difference between the deep and the shallow ratios; the blue curves are closer to one another than the red curves in Figure 5d and 5e. In the case of constant attenuation with depth (Figure 5f) but increasing stress drop, the

difference between the two blue curves is little different from that between the two red ones; the small difference results from the varying corner frequency of the smaller EGF events because of the depth-dependent stress drop.

The bottom row of Figure 5 essentially shows the ratios of the deep to shallow earthquake spectra with (blue) and without (red) a correction for depth-dependent attenuation. These correspond to the ratio of the two blue ratios and the two red ratios shown in the middle row. The triangles of the same color indicate the mean value of the ratios in the frequency range 2-20 Hz, typical of the studies used in our analysis. When stress drop is constant, but $Q$ increases with depth (Figure 5g) the blue ratio is close to one, systematically lower than the red ratio. When both stress drop and $Q$ increase with depth (Figure 5h) then the blue ratio is larger than one, but systematically lower than the red ratio. When stress drop increases with depth, but $Q$ is constant (Figure 5i) then there is no difference between the two ratios, except near and above the EGF corner frequency.

For clarity in this simple example, we implicitly assume that both the shear wave velocity and the rupture velocity are constant, independent of depth. If the rupture velocity increases with depth, perhaps as a constant function of shear wave (or even P wave) velocity, then this would cause a deeper earthquake to have a higher corner frequency than a shallower one, even if they both had the same stress drop. Hence, a constant stress drop with depth could look more like the middle, or even the righthand columns of Figure 5, depending on the rate of increase in rupture velocity with depth.

We use the EGF-based approach described above to investigate the event spectra from the different spectral decomposition studies. For each region, we stack the event spectra in different magnitude and depth bins (by calculating the mean of the log spectral amplitudes), calculate ratios between large and small events and compare the results to the middle and bottom rows of Figure 5. For simplicity, we first focus on the systematic variation in the ratios and corner frequencies. In the Discussion, we explicitly look at the effects of including varying rupture velocity. We use the consistent color scheme introduced in Figures 4 and 5 throughout the paper to improve clarity.

## 6.2 Application to Data

To investigate the causes of the varying spectral shape with source depth observed in the data (Figure 2 and 3) we stack the event spectra for all the earthquakes in magnitude and depth bins to obtain stable mean spectra that we can compare following the approach outlined in the synthetic test (Figure 5). We stack the data to focus on the systematic effects common to a population of events, rather than the variation between individual earthquakes.

For each study we select a shallow depth range and a deep depth range (Table 1). These depths are guided by the observed changes with depth of both the frequency content of the event spectra and the velocity structure (Figure 3), and the need for sufficient earthquakes in the two depth ranges for stable stacking. We perform our analysis comparing earthquakes from these two depth ranges, but to ensure that our results are not dependent on these selected values, we also repeat the entire analysis simply dividing each data set at its median value into a shallower and deeper event population. We do not try using the same depth ranges for different data sets because the different earthquake populations have very different depth distributions (Figure 3). Source spectral shape depends on earthquake magnitude and so we divide the earthquakes into bins of 0.2Mw units to enable the averaging of stacking.

For each dataset, we stack the event spectra in each magnitude and depth bin by calculating the geometric mean spectrum for each bin. We then calculate the ratios between pairs of large and small (EGF) events as described in the synthetic example. For the ratios without any depth correction, we include earthquakes from the entire depth range of the study (not just the deep and shallow ranges) in the stack of small EGF events. We try all available magnitude bins, but only use those with at least 5 large and 5 small events. The results for the Ridgecrest aftershock sequence are shown in Figure 6, and the results of other example data sets are shown in the Supporting Information (Figure S4). We select the magnitude bin for the EGF events in two different ways. First, we use a constant magnitude difference (0.8 Mw units) between the large and small events (top two rows of Figure 6). Second, we select one fixed Mw bin as the preferred EGF and apply it to all Mw bins at least 0.8 Mw units larger (bottom row in Figure 6). One magnitude pairing is therefore included in both (Mw2.6/Mw1.8 in Figure 6). We apply the two approaches to ensure that our results are not dependent on the method of selecting the EGF, and they are also useful as a check on the uncertainties in our analysis. Clearly if earthquakes of

different depth, in any Mw bin, have different stress drops, then this will be true regardless of the exact magnitude of the EGF events.

Each panel of Figure 6 can be compared directly to Figure 5d,e,f, to distinguish between depth-dependent source and path effects. In all panels of Figure 6, the difference between the source spectral ratios for deep and shallow events decrease when depth-specific EGF corrections are applied. In some cases, the deep and shallow spectral ratios become almost indistinguishable (e.g., Mw3.2/Mw2.4) when using depth-specific EGFs, resembling Figure 5d in which all the depth dependence is a consequence of attenuation. Most panels of Figure 6 more closely resemble Figure 5e, exhibiting a significant decrease in depth dependence when using depth-specific EGFs.

We then fit the spectral ratios (as shown in Figure 6) using the Brune source model:

$$\frac{X_1(f)}{X_2(f)} = \frac{e_1(f)}{e_2(f)} = \frac{M_{0}1}{M_{0}2}\frac{\left[1+\left(\frac{f}{f_{c}2}\right)^2\right]}{\left[1+\left(\frac{f}{f_{c}1}\right)^2\right]} \qquad (3),$$

which has been shown to work well for stacked spectra (e.g., Shearer *et al*., 2006; 2019); subscripts 1 and 2 refer to the larger event stack and the smaller event stack, respectively. Many of the datasets we consider are unlikely to have sufficient resolution to separate completely the path and source effects (e.g., Shearer *et al.*, 2019), and so we fix the corner frequency of the stacked EGF events (denominator) in the spectral ratios ($f_{c^2}$). We first assume a stress drop of 3 MPa (e.g., Abercrombie 1995, Shearer *et al*. 2006) for the smaller stacked events, and calculate the corner frequency following Madariaga (1976) and Eshelby (1957)

$$f_{c^2} = k\beta\left(\frac{16\Delta\sigma}{7M_{0}2}\right)^{1/3} \qquad (4)$$

assuming $k$=0.32 and an average shear wave velocity, $\beta$=3500 m/s, for all depth bins and data sets. These fits are shown in Figure 6, and for other example data sets in the Supporting Information (Figure S4). We then try different values to investigate their effects on our results, as discussed in the next section. We do not expect our analysis to obtain the actual stress drops of the various event stacks; rather, we use the spectral ratio modeling simply to quantify the systematic patterns that can distinguish between depth dependent source and path effects.

## 7 Results and Discussion

The aim of our analysis is to distinguish between depth dependent source and path effects within the event spectra obtained by spectral decomposition, which in turn is based on a simplified approximation of path-dependent attenuation. Our results are also relevant to any EGF-based analysis, whether in the frequency or time domain, indicating that depth should be included as a constraint in the selection of EGF events (e.g., Abercrombie 2015). Our approach involves comparing stacks of deep and shallow earthquake event spectra, divided by smaller stacked EGF earthquakes selected either from the same depth ranges (depth-specific EGFs to correct for depth-dependent path effects) or averaged over the entire depth range (no correction for depth-dependent path effects). Figure 6 shows how using depth-specific EGFs systematically decreases the differences between the shallow and deep source spectra. Figures 7-9 show the results for the datasets with the most earthquakes (see Table 1 for numbers) which are most robust, and also for the Hayward fault analysis by Hardebeck and Aron (2009) that found a strong increase in stress drop with depth. Following the color scheme in Figure 4 and 5, blue symbols represent measurements made with a correction for depth-dependent path effects (i.e., depth-specific EGFs) and red symbols represent measurements without a correction for depth-dependent path effects. The results from all the datasets are shown in the Supporting Information (Figures S5-8).

Figure 7 compares the ratios of the deep and shallow, stacked, EGF-corrected, event spectra for different magnitude bins, and can be understood by direct comparison with Figure 5g,h,i. In most regions the red ratios (deep, EGF corrected / shallow, EGF corrected, where EGFs are independent of source depth) increase with frequency, suggesting the deeper earthquakes may contain more higher frequency energy than similar sized shallow events, but this difference is systematically reduced by the use of depth-specific EGF events (blue curves: deep, EGF corrected / shallow, EGF corrected, where EGFs are depth specific). This effect is strongest in the Ridgecrest and Parkfield datasets. Comparison of Figure 7 with the synthetic examples in Figure 5, shows most similarity with panels 5d and 5e; this implies that using EGFs from the correct depth range can remove a significant amount of the apparent difference between deep and shallow earthquake sources.

To quantify the effect of the different EGF corrections, we calculate the mean values of each of the blue and red (with and without including depth-specific EGF corrections) ratios (Figure 8,

S6) in the frequency range 2-20 Hz. These results can be directly compared to the synthetic models in Figure 5g,h,i. In each study, the amplitudes of the ratios without including an EGF correction for source depth (red symbols) are systematically higher than those that do use depth-specific EGFs (blue symbols); the effect is weaker in datasets that exhibit little depth-dependence of any kind. There is no obvious reason why any real increase in either source properties or $Q$ with depth would depend on either the magnitude of the larger events, or the magnitude of the EGF events. Any variation between the different symbols of the same color is more likely to represent uncertainties and variability from small populations of earthquakes, and the simplifying assumptions used in the stacking. We interpret the observation that the blue symbols using depth-specific EGFs are systematically closer to one in all cases, to indicate that much of the apparent difference in deep and small earthquakes observed in event spectra is an artefact of not including depth-dependent attenuation in the inversion.

The spectral ratio fitting confirms this result. Figures 9 and S7 show that after correction with the depth-specific EGF events, any increase in corner-frequency with depth becomes systematically smaller, and almost negligible. Again, the variability of symbols of a given color indicates the uncertainties in the measurements.

## 7.1 Effect of Depth Range Selection

These results are all based on selecting representative depth ranges for the shallow and deep earthquake populations. Although these selections are based on the velocity structures and the earthquake depth distributions, they are somewhat arbitrary and subjective. To ensure that they are not strongly influencing the results, we repeat the entire analysis, but instead of selecting the depth ranges, we simply divide each of the earthquake populations in half at their respective median depths. As shown in Figure S8a, there is a small reduction in the effects of using the correction for depth-specific EGFs, compared to Figure 9. This is expected as the two populations compared in Figure S8a include more intermediate depth events and are less distinct. The general observation of decreasing difference (between shallow and deep earthquakes) following application of depth-specific EGFs remains clear and consistent across the entire dataset indicating that our precise choices of depth are not affecting our main conclusion.

## 7.2 Effect of Spectral Fitting Assumptions

The comparisons using spectral fitting are consistent with the basic spectral observations in Figures 7 and 8, but do involve assumptions and constraints that may affect the results. One significant assumption is the value to which we fix the corner frequency of the EGF events ($f_{c2}$) in the ratios. The limited bandwidth of most of the data means that $f_{c2}$ is very unlikely to be resolvable as a free parameter (e.g., Abercrombie, 2015; Ruhl *et al*., 2017; Shearer *et al*., 2019); the majority of fixed and inverted $f_{c2}$ values are between 10 and 40 Hz. In our analysis, we assume that $f_{c2}$ is independent of the depth of the EGF earthquakes, and it is possible that this assumption of depth independence may affect our modeling of the depth-dependence of the larger earthquakes. We therefore perform a series of inversions to investigate the constraints and tests to determine whether our results could be significantly biased by our assumptions.

First, we consider using a mean stress drop that is three times higher to calculate all values of $f_{c2}$, regardless of depth. This results in an almost identical variation with depth to that found with 3 MPa and shown in Figure 9. This forced higher stress drop for the smaller earthquakes resulted in consistently higher corner frequencies and stress drops for the larger earthquakes, but also significantly higher misfit variance in almost all datasets (Figure S9).

Second, we try fixing the stress drop of the deep earthquakes used to calculate $f_{c2}$ to be a factor of 2, 3 or 5 higher than that assumed for the shallower groups of earthquakes. (This test also addresses the effects of an increasing velocity with depth causing an increasing $f_{c2}$ with depth even if stress drop is constant.) This resulted in the depth-specific EGF correction removing less of the depth dependence to the stress drop for the larger earthquakes (e.g., Figure S8b). Comparison of the misfit variances from these tests (Figure S9) shows that, on average, the observed spectral ratios in all datasets are consistently fit better with a constant stress drop for the smaller EGF earthquakes, independent of depth, than with the depth-dependent assumption. This is consistent with the visual comparison of the observed event spectral ratios in Figures 6 and 7.

Finally, we also try allowing $f_{c2}$ as a free variable in the spectral ratio fitting, but, as expected, find the results to be unconstrained. We conclude this using the same approach as Shearer *et al*. (2019). Stacked event spectra of the same smaller earthquakes, from all depths, are used as EGFs for both deep and shallow earthquakes, when the effects of a depth correction are

ignored. We obtain systematically different values for $f_{c2}$ for the same event stack when it is used as the denominator for deep and shallow larger events. We do not know which value of $f_{c2}$ is correct, but we do know that the same set of earthquakes should have the same absolute value, independent of the events to which it is compared. Therefore, the different values obtained indicate the lack of constraint in the spectral fitting, and so we limit our interpretations to the results of fitting with fixed values of $f_{c2}$.

## 7.3 Relationship between Attenuation and Velocity Structure

In Figure 3 we compare the variation with depth of the average spectral shape of earthquakes in each region with the local P-wave velocity structure. Although the S wave velocity is used in equation 4, all the spectra used in this analysis are calculated from P waves. Event spectra that extend over a wider range of source-region velocity appear to show higher variation in frequency content. Since both attenuation and velocity are related to material properties of the structure, then some relation between them is expected. For example, Brocher (2008) and Eberhart-Phillips *et al*. (2015) showed that $Q$ increases with velocity but there is considerable scatter and no simple relationship.

In Figure 10 we compare the corner frequencies of deep and shallow earthquakes of the same magnitude, calculated assuming fixed, depth-independent, $f_{c2}$, to the source region velocity. We calculate the mean velocity in the depth range of the events in each population used in the spectral ratios, using the structures in Table 1 and Tables S1-10. We then plot the ratio of the deep and shallow source parameters against the ratio of the deep to shallow source velocity for each spectral ratio. All points from regions with two alternative velocity models (for example, both sides of the Hayward fault) are plotted twice. Figure 10a shows the relationship without using the depth-specific EGFs; there is a large scatter, but a general increase in apparent corner frequency difference with increasing velocity difference can be seen. This increase is larger than could be explained by a constant stress drop, even allowing the rupture velocity to increase proportional to the P wave velocity (equation 4, dashed line in Figure). Figure 10b shows the same results after the spectral ratios are corrected using the depth-specific EGFs. The differences with depth are smaller, and no longer show any obvious dependence on source depth. Most of the variability is within the range that could be explained by increasing rupture velocity with depth. This comparison suggests that although the velocity structure is inadequate for a real

estimate of attenuation, variation in velocity with depth could be used as a first order indication of the depth-dependence of the attenuation (e.g., Eberhart-Phillips *et al*., 2016). Also, if the difference in velocity with depth is known, then Figure 10 provides a guide to the size of the effect depth-dependent attenuation could have on estimates of corner frequency.

## 7.4 Implications for Depth Dependence of Earthquake Stress Drop

Our analysis has shown that the increase in $Q$ with depth can exert a first order effect on recorded seismograms, that cannot be ignored when investigating changes in stress drop with depth. This result is in good agreement with the earlier studies of Edwards *et al.* (2008) and Edwards and Rietbrock (2009) who demonstrated the effects of including depth dependent attenuation on stress drop measurements. Our analysis implies that much, if not all, the increase in stress drop with depth reported by previous spectral decomposition studies could be an artefact caused by inadequate consideration of depth-dependent attenuation.

As pressure, and hence normal stress, increases with depth in the earth, it seems reasonable that the stress release in earthquakes should increase also (e.g., Sibson, 1974; Scuderi *et al.,* 2016). Otherwise, the differential stresses involved in faulting must somehow remain constant, despite the increasing pressure, or the deeper earthquakes must release a smaller fraction of the peak differential stress. Whether we can resolve real increase in stress drop with depth from existing earthquake recordings remains open to question. Like previous work, our results are also subject to uncertainties, and depend on assumptions about the corner frequency of the smallest earthquakes, and so some increase in stress drop with depth is well-within the constraints. In the future, further work is required at the interface of attenuation tomography and source modeling to investigate the real resolution of both, and to balance the need to account for spatially (and temporally) varying attenuation, and different source geometries, without increasing the number of free parameters well beyond the constraints of the available data.

To investigate resolution, and spatial variability, Pennington *et al*. (2021) performed a detailed comparison of multiple methods of calculating stress drop. To address the possibility of depth dependent attenuation in spectral decomposition approaches, they calculated different empirical correction spectra for the earthquakes in the basement to those in the overlying sediments. This significantly decreased the depth dependence of the resulting stress drop estimates. They found best agreement between the various studies in the central depth range of

606 the events, within the upper kilometers of the basement. Zhang *et al.* (2019) investigated the
607 effects of using separate empirical correction spectra for earthquakes in different depth ranges in
608 their spectral decomposition analysis of borehole-recorded earthquakes at Parkfield. They too
609 found that after including changes in $Q$ with depth, only negligible change in stress drop with
610 depth remained. Ruhl and Abercrombie (2020) implemented a similar approach for the Mogul
611 earthquakes, and obtained similar results that are consistent with the detailed, smaller scale EGF
612 analysis by Ruhl *et al.* (2017) which found no significant depth dependence to stress drop. These
613 studies are a first step towards improving resolution of the trade-off between source and path in
614 spectral decomposition analyses, without simply adding so many free parameters as to make the
615 whole problem completely unconstrained. Using depth-dependent correction functions to
616 account for changes in $Q$ with depth is not fully satisfactory, however, as it comes after the initial
617 spectral decomposition in which the path terms are assumed to be independent of source depth,
618 and only depend on travel time.
619 Similar to the original empirically-corrected spectral decomposition analyses, the results
620 of the generalized inversion studies such as Bindi *et al*. (2020a) and Oth *et al*. (2011) do not
621 explicitly consider an increase in $Q$ with source depth. They too should be considered potentially
622 biased in the same manner as the spectral decomposition analyses. For example, at Ridgecrest
623 Bindi *et al*. (2020b) obtained a similar apparent depth dependence to stress drop as Trugman
624 (2020) and also did not explicitly consider an increase in $Q$ with source depth. Bindi *et al.* (2021)
625 performed a subsequent study and identified a combination of depth and distance varying
626 attenuation and stress drop increasing with depth that were able to fit the observed spectra. Given
627 the large trade-offs among the parameters this is not surprising, and they did not investigate the
628 uniqueness of their solution. Bindi *et al*. (2020; 2021) also used variable time windows, each
629 incorporating different combinations of $P$, $S$ and coda energy, which makes it hard to compare
630 their results directly with the short $P$-wave windows used in the present analysis. Parker *et al*.
631 (2020) investigated the performance of ground motion prediction equations on the aftershocks of
632 the 2019 Ridgecrest earthquake and observed that the deeper earthquakes exhibited higher
633 ground acceleration, consistent with their having higher stress drop. Like the studies by Trugman
634 (2020) and Bindi *et al*. (2020b) of the same sequence, they did not include any dependence of
635 attenuation on source depth in their analysis. In empirical ground motion prediction, it is not
636 essential to distinguish whether source or path effects cause a trend when interpolating within a

637 data set, but it is required to extrapolate predictions to different regions, or larger magnitude
638 earthquakes (e.g., Bommer *et al*., 2007).

639 The results of empirical Green's function studies in which a collocated small earthquake
640 is used to compensate for all the path and site effects should, theoretically, be unaffected by the
641 tradeoffs between attenuation and source. In practice, however, the lack of suitable EGF events,
642 and uncertainties in their locations (especially depth) mean that often an EGF may not fully
643 compensate for the attenuation. Abercrombie (2015) and Kane *et al*. (2013) showed how EGF
644 selection can affect stress drop measurements; clearly if the EGF is imperfect, then not only will
645 the source spectral shape be biased, but the duration of the source time function will also be
646 affected, and so time-domain measurements are not immune to this trade-off. Huang *et al.* (2017)
647 and Boyd *et al*. (2017) both used spectral ratio approaches to investigate stress drop dependence
648 on depth and tectonic setting, but had insufficient earthquakes to only use EGFs of similar depth
649 to the main events. Boyd *et al*. (2017) included the effects of increasing velocity and rigidity
650 with depth on the estimates of seismic moment, rupture velocity and hence stress drop, finding
651 that stress drop increased with depth. However, in their cluster-based analysis, they combined
652 earthquakes from a similar range of depths and velocities as the analyses revisited here, making
653 no correction for the different source depths. It is possible, therefore, that the increase in stress
654 drop with depth that they reported is an artefact, or over-estimate. Unlike the other studies
655 discussed, Boyd *et al*. (2017) used coda wave spectra in their analysis. Mayeda *et al*. (2007)
656 showed that coda wave measurements are more stable, and less sensitive to spatial separation
657 between main and EGF events than direct wave measurements, but they did not specifically
658 consider separation in source depth. Coda wave generation is observed to vary with depth,
659 especially in the shallow layers of the crust (e.g., Voyles *et al.,* 2019). Walter *et al*. (2017)
660 included source depth in their selection of earthquakes for coda wave spectral ratio analysis in
661 Oklahoma. They observed an increase in stress drop with depth too large to be easily explained
662 as an artifact of attenuation or velocity structure, but for only a relatively small number of events.
663 Trugman and Savvaidis (2021) observed no clear depth-dependence in stress drop for seismicity
664 in the Pecos area of west Texas, though the large depth uncertainties of earthquakes recorded in
665 this region at present renders this finding unsurprising.

## 8 Conclusions

We investigate whether the increases in stress drop with depth reported by spectral decomposition earthquake studies are real, or potentially an artefact of neglecting to correct sufficiently for depth variation in attenuation ($Q$). We combine the event spectra calculated for over 50,000 earthquakes (M0-5) from 12 studies in California, Nevada, Kansas, and Oklahoma. We analyze spectral ratios between large and small events as a function of source depth, to explore the relative importance of source and attenuation contributions to the observed depth dependence in high-frequency radiation and corner frequency.

We find that correcting the earthquake event spectra with depth-specific empirical Green's functions can remove most, if not all, of the apparent stress drop increase with depth previously observed in the original studies. The largest corrections are observed in regions with the largest velocity increase with depth. We conclude that source spectral analyses, whether using spectral decomposition, empirical Green's functions, or any other approach, should not assume path terms are independent of source depth. More explicit depth-dependent attenuation models or depth-specific empirical corrections are required to resolve real variation of earthquake source processes with depth in the earth.

## 9 Data and Resources

This study uses the event spectra calculated in the published studies listed in Table 1, and cited in the References. The original waveforms are available from the Southern California Earthquake Data Center (SCEDC (2013): Southern California Earthquake Center (SCEC), Caltech, Dataset, doi:10.7909/C3WD3xH1. The SCEDC and Southern California Seismic Network (SCSN) are funded through U.S. Geological Survey Grant G20AP00037, and SCEC), the Northern California Earthquake Data Center (NCEDC), doi:10.7932/NCEDC, including the High Resolution Seismic Network (HRSN) doi:10.7932/HRSN, operated by the UC Berkeley Seismological Laboratory, and the Nevada Seismic Network (https://doi.org/10.7914/SN/NN). The other waveforms are available from IRIS, as follows: https://doi.org/10.7914/SN/GS; UC San Diego. (2013). *Central and Eastern US Network*. International Federation of Digital Seismograph Networks (IFDSN). https://doi.org/10.7914/SN/N4; USGS Earthquake Science Center (2009). *NetQuakes*. IFDSN. https://doi.org/10.7914/SN/NQ; Darold (2014) 4D Integrated

Study Using Geology, Geophysics, Reservoir Modeling & Rock Mechanics to Develop Assessment Models for Potential In., IFDSN. https://doi.org/10.7914/SN/ZD_2014; Oklahoma Geological Survey, 1978. Oklahoma Seismic Network, IFDSN, https://doi-org./10.7914/SN/OK; Nanometrics Seismological Instruments, 2013. Nanometrics Research Network, IFDSN, https://doi-org/10.7914/SN/NX. The velocity structures used are cited in Table 1, and included in the Supporting Information

## 10 Acknowledgements

We are grateful to Malcolm White and Evan Hirakawa for extracting the representative 1D velocity models in the relevant regions of southern and northern California, respectively. Discussions with Donna Eberhart-Phillips and Annemarie Baltay, and reviews by Yihe Huang (Associate Editor), Oliver Boyd and two anonymous reviewers greatly improved the manuscript. This work was supported by funding from SCEC (Awards 19163 and 20097). SCEC is funded by NSF Cooperative Agreement EAR-1033462 and USGS Cooperative Agreement G12AC20038. This is SCEC publication number 11037.

## 11 References

Aagaard, B.T., Graymer, R.W., Thurber, C.H., Rodgers, A.J., Taira, T., Catchings, R.D., Goulet, C.A., & Plesch, A. (2020). Science plan for improving three-dimensional seismic velocity models in the San Francisco Bay region, 2019–24: U.S. Geological Survey Open-File Report 2020–1019, 37 p., https://doi.org/10.3133/ofr20201019.

Abercrombie, R. E. (1995), Earthquake source scaling relationships from -1 to 5 *ML*, using seismograms recorded at 2.5 km depth, *Journal of Geophysical Research: Solid Earth., 100*, 24015-24036.

Abercrombie, R. E. (1997). Near surface attenuation and site effects from comparison of surface and deep borehole recordings, *Bulletin of the Seismological Society of America, 87*, 731-744.

Abercrombie, R. E. **(**2015). Investigating Uncertainties in Empirical Green's Function Analysis Earthquake Source Parameters, *Journal of Geophysical Research: Solid Earth,* 120, 4263–4277, doi: 10.1002/2015JB011984**.**

723 Abercrombie, R. E. (2021). Resolution and Uncertainties in Estimates of Earthquake stress drop
724 and Energy Release, *Philosophical Transactions of the Royal Society A,* 379, 20200131.
725 20200131. *http://doi.org/10.1098/rsta.2020.0131*
726 Abercrombie, R. E., S. Bannister, J. Ristau, & D. Doser, (2017). Variability of Earthquake Stress
727 Drop in a subduction setting, the Hikurangi Margin, New Zealand, *Geophysical Journal*
728 *International*, 208, 306-320, doi:10.1093/gji/ggw393.
729 Allmann, B. P., & Shearer, P. M. (2007). Spatial and temporal stress drop variations in small
730 earthquakes near Parkfield, California. *Journal of Geophysical Research: Solid Earth, 112*,
731 B04305. doi:10.1029/2006JB004395
732 Anderson J. G., & Hough S. E. (1984). A model for the shape of the Fourier amplitude spectrum
733 of acceleration at high frequencies. *Bulletin of the Seismological Society of America*, 74,
734 1969–1993.
735 Bindi, D., Hoby N. T. Razafindrakoto, M. Picozzi & A. Oth (2021). Stress Drop Derived from
736 Spectral Analysis Considering the Hypocentral Depth in the Attenuation Model: Application
737 to the Ridgecrest Region, California. *Bulletin of the Seismological Society of America*,
738 doi: https://doi.org/10.1785/0120210039
739 Bindi, D., D. Spallarossa, M. Picozzi & P. Morasca (2020a). Reliability of Source Parameters for
740 Small Events in Central Italy: Insights from Spectral Decomposition Analysis Applied to
741 Both Synthetic and Real Data, *Bulletin of the Seismological Society of*
742 *America* ., 10.1785/0120200126.
743 Bindi, D., R. Zaccarelli, &S. R. Kotha (2020b). Local and Moment Magnitude Analysis in the
744 Ridgecrest Region, California: Impact onInterevent Ground-Motion Variability, *Bulletin of*
745 *the Seismological Society of America*.111, 339–355, doi: 10.1785/0120200227
746 Bommer, J. M., P. J. Stafford, J. E. Alarcón & S. Akkar (2007). The Influence of Magnitude
747 Range on Empirical Ground-Motion Prediction. *Bulletin of the Seismological Society of*
748 *America*, 97 (6): 2152–2170. doi: https://doi.org/10.1785/0120070081
749 Boyd, O. S., D. E. McNamara, S. Hartzell & G. Choy (2017). Influence of Lithostatic Stress on
750 Earthquake Stress Drops in North America. *Bulletin of the Seismological Society of America*,
751 107 (2): 856–868. doi: https://doi.org/10.1785/0120160219
752 Brocher, T. M. (2008) Key elements of regional seismic velocity models for long period ground
753 motion simulations. *J Seismol 12,* 217–221. https://doi.org/10.1007/s10950-007-9061-3

754 Brune, J. (1970). Tectonic stress and the spectra of seismic shear waves from earthquakes,
755 *Journal of Geophysical Research*, 75, 4997-5009.
756 Byerlee, J. D., & Brace, W. F. (1968). Stick slip, stable sliding, and earthquakes-effect of rock
757 type, pressure, strain rate, and stiffness. *Journal of Geophysical Research*, *73*(18), 6031–
758 6037.
759 Chen, C. (2016). Comprehensive analysis of Oklahoma earthquakes: From earthquake
760 monitoring to 3D tomography and relocation (PhD dissertation). University of Oklahoma.
761 Chen, X., & Shearer, P. M. (2011). Comprehensive analysis of earthquake source spectra and
762 swarms in the Salton Trough, California, *Journal of Geophysical Research: Solid Earth*, 116,
763 B09309, doi:10.1029/2011JB008263
764 Chen, X., & R E Abercrombie, (2020). Improved approach for stress drop estimation and its
765 application to an induced earthquake sequence in Oklahoma, *Geophysical Journal*
766 *International,* 223, 1, 233-253. doi:10.1093/gji/ggaa316
767 Dieterich, J. H. (1979). Modeling of rock friction: 1. Experimental results and constitutive
768 equations. *Journal of Geophysical Research*, *84*(9), 2161–2168. Retrieved from
769 http://dx.doi.org/10.1007/BF00876539
770 Eberhart-Phillips, D. (2016). Northern California Seismic Attenuation: 3D *QP* and *QS* Models.
771 *Bulletin of the Seismological Society of America,* 106, 2558–2573. doi:10.1785/0120160060
772 Eberhart-Phillips, E., Reyners, M., & Bannister, S. (2015). A 3D *QP* Attenuation Model for All
773 of New Zealand. *Seismological Research Letters* 86, 1655–1663. doi:10.1785/0220150124
774 Edwards B. & Rietbrock A. (2009). A comparative study on attenuation & source-scaling
775 relations in the Kanto, Tokai, & Chubu Regions of Japan, using data from Hi-Net & Kik-Net,
776 *Bulletin of the Seismological Society of America*, 99, doi:10.1785/0120080292
777 Edwards B. Rietbrock A. Bommer J.J. & Baptie B. (2008). The acquisition of source, path and
778 site effects from micro-earthquake recordings using *Q* tomography: application to the UK,
779 *Bulletin of the Seismological Society of America*, 98, 1915–1935.
780 Eshelby, J. D., (1957). The determination of the elastic field of an ellipsoidal inclusion and
781 related problems. *Proceedings of the Royal Society of London, A, 241*, 376-396.
782 Goebel,T. H. W., E. Hauksson, P.M. Shearer & J.P. Ampuero (2015). Stress-drop heterogeneity
783 within tectonically complex regions: a case study of San Gorgonio Pass, southern
784 California, *Geophysical Journal International*, 202, 514–528. doi:10.1093/gji/ggv160

785 Goertz-Allmann, B. P. & B. Edwards (2014). Constraints on crustal attenuation and three-
786 dimensional spatial distribution of stress drop in Switzerland, *Geophysical Journal*
787 *International*, 196, 493–509, doi:10.1093/gji/ggt384
788 Hardebeck, J. L. (2020). Are the stress drops of small earthquakes good predictors of the stress
789 drops of moderate-to-large earthquakes? *Journal of Geophysical Research: Solid Earth*, 125,
790 e2019JB018831. doi:10.1029/2019JB018831
791 Hardebeck, J. L. & A. Aron, (2009). Earthquake Stress Drops and Inferred Fault Strength on the
792 Hayward Fault, East San Francisco Bay, California. *Bulletin of the Seismological Society of*
793 *America*, 99, 1801-1814.
794 Hauksson, E., & Shearer, P. M. (2006). Attenuation models ($Q_P$ and $Q_S$) in three dimensions of
795 the southern California crust: Inferred fluid saturation at seismogenic depths, *Journal of*
796 *Geophysical Research: Solid Earth*, 111, B05302, doi:10.1029/2005JB003947.
797 Hough S. E. & Anderson J. G. (1988). High-frequency spectra observed at Anza, California:
798 implications for Q structure, *Bulletin of the Seismological Society of America 78*, 692- 707.
799 Huang, Y., W. L. Ellsworth & G. C. Beroza, (2017). Stress drops of induced and tectonic
800 earthquakes in the central United States are indistinguishable, *Science Advances*, 3,
801 e1700772, doi: 10.1126/sciadv.1700772
802 Kane, D.L., D.L. Kilb, & F.L. Vernon (2013), Selecting Empirical Green's Functions in Regions
803 of Fault Complexity: A Study of Data From the San Jacinto Fault Zone, Southern California,
804 *Bulletin of the Seismological Society of America 103*, no. 2A, doi: 10.1785/0120120189.
805 Kaneko, Y. & Shearer, P. M. (2015). Variability of seismic source spectra, estimated stress drop,
806 and radiated energy, derived from cohesive-zone models of symmetrical and asymmetrical
807 circular and elliptical ruptures. *Journal of Geophysical Research: Solid Earth, 120*,
808 1053– 1079. doi: 10.1002/2014JB011642
809 Lomax, A. (2020). Absolute Location of 2019 Ridgecrest Seismicity Reveals a Shallow Mw 7.1
810 Hypocenter, Migrating and Pulsing Mw 7.1 Foreshocks, and Duplex Mw 6.4
811 Ruptures. *Bulletin of the Seismological Society of America,* 110 (4): 1845–1858.
812 doi:10.1785/0120200006
813 Madariaga, R. (1976). Dynamics of an expanding circular crack, *Bulletin of the Seismological*
814 *Society of America*, *66*, 639-666.

Marone, C. (1998). Laboratory-derived friction laws and their application to seismic faulting. *Annual Reviews of Earth and Planetary Science*, *26*, 643–696.

Marty, S., Passelègue, F. X., Aubry, J., Bhat, H. S., Schubnel, A., & Madariaga, R. (2019). Origin of high-frequency radiation during laboratory earthquakes. *Geophysical Research Letters*, 46, 3755– 3763. https://doi-org/10.1029/2018GL080519

Mayeda, K., L. Malagnini & W. R. Walter (2007). A new spectral ratio method using narrow band coda envelopes: Evidence for non-self-similarity in the Hector Mine *Geophysical Research Letters*, 34, L11303, doi:10.1029/2007GL030041.

Oth, A., D. Bindi, S. Parolai & D. Di Giacomo (2011). Spectral analysis of K-NET and KiK-net data in Japan, Part II: On attenuation characteristics, source spectra, and site response of borehole and surface stations. *Bulletin of the Seismological Society of America,* 101, 667-687, doi: 10.1785/0120100135.

Parker, P. A., A. S. Baltay, J. Rekoske & E. M. Thompson (2020). Repeatable Source, Path, and Site Effects from the 2019 **M**M 7.1 Ridgecrest Earthquake Sequence, *Bulletin of the Seismological Society of America,* 110 (4): 1530–1548. doi: doi.org/10.1785/0120200008

Pennington, C., X. Chen, R. W. Abercrombie & Q. Wu (2021). Cross Validation of Stress Drop Estimates and Interpretations for the 2011 Prague, OK, Earthquake Sequence Using Multiple Methods, *Journal of Geophysical Research: Solid Earth, 126, e2020JB020888.* https://doi.org/10.1029/2020JB020888

Prieto, G. A., Shearer, P. M., Vernon, F. L., & Kilb, D. (2004). Earthquake source scaling and self-similarity estimation from stacking P and S spectra, *Journal of Geophysical Research: Solid Earth,* 109, B08310, doi:10.1029/2004JB003084.

Ross, Z. E., Kanamori, H., and Hauksson, E. (2017). Anomalously large complete stress drop during the 2016 $M_w$ 5.2 Borrego Springs earthquake inferred by waveform modeling and near-source aftershock deficit, *Geophysical Research Letters*, 44, 5994– 6001, doi:10.1002/2017GL073338.

Rubinstein, J. L., W. L. Ellsworth & S. L. Dougherty (2018). The 2013–2016 Induced Earthquakes in Harper and Sumner Counties, Southern Kansas. *Bulletin of the Seismological Society of America,* 108 (2): 674–689. doi:10.1785/0120170209

Ruhl, C. J., & Abercrombie, R. E. (2020). Systematic Fault Plane Analysis in Complex Earthquake Sequences: Application to the 2019 Ridgecrest, CA and 2008 Mogul, NV Earthquakes. Poster Presentation at 2020 SCEC Annual Meeting.

Scuderi, M. M., Marone, C., Tinti, E., Di Stefano, G., & Collettini, C. (2016). Precursory changes in seismic velocity for the spectrum of earthquake failure modes. *Nature Geoscience*, *9*(9), 695–700. https://doi.org/10.1038/ngeo2775

Shaw, J. H., A. Plesch, C. Tape, M. P. Suess, T. H. Jordan, G. Ely, E. Hauksson, J. Tromp, T. Tanimoto, R. Graves, K. Olsen, C. Nicholson, P. J. Maechling, C. Rivero, P. Lovely, C. M. Brankman, & J. Munster (2015). Unified Structural Representation of the southern California crust and upper mantle. *Earth and Planetary Science Letters*. 415 1, doi: 10.1016/j.epsl.2015.01.016

Shearer, P. M., & R. E. Abercrombie **(**2021). Calibrating Spectral Decomposition of Local Earthquakes using Borehole Seismic Records - Results for the 1992 Big Bear Aftershocks in Southern California, *Journal of Geophysical Research: Solid Earth, 126, e2020JB020561.* https://doi.org/10.1029/2020JB020561

Shearer, P. M., R. E. Abercrombie, D. T. Trugman & W. Wang (2019). Comparing EGF Methods for Estimating Corner Frequency and Stress Drop from P Wave Spectra. *Journal of Geophysical Research: Solid Earth*, 124, 4, 3966-3986. doi:10.1029/2018JB016957

Shearer, P. M., G. A. Prieto, & E. Hauksson (2006). Comprehensive analysis of earthquake source spectra in Southern California, *Journal of Geophysical Research: Solid Earth*, **111**, B06303, doi:10.1029/2005JB003979.

Sibson, R. H. (1974). Frictional constraints on thrust, wrench and normal faults. *Nature*, *249*(5457), 542–544. https://doi.org/10.1038/249542a0

Small, P., Gill, D., Maechling, P. J., Taborda, R., Callaghan, S., Jordan, T. H., Ely, G. P., Olsen, K. B., & Goulet, C. A. (2017). The SCEC Unified Community Velocity Model Software Framework. *Seismological Research Letters*, 88(5). doi:10.1785/0220170082.

Toth, C. R., Holland, A. A., Keranen, K. M., & Gibson, A. (2012). Relocation and comparison of the 2010 M 4.1 and 2011 M 5.6 earthquake sequences in Lincoln County, Oklahoma. In Eastern section SSA 2012 annual meeting. Blacksburg, Virginia, 28-30 October 2012.

873 Trugman, D. T. (2020). Stress-Drop and Source Scaling of the 2019 Ridgecrest, California,
874 Earthquake Sequence, *Bulletin of the Seismological Society of America*, 110, 1859–1871.
875 doi:10.1785/0120200009.
876 Trugman, D. T., Dougherty, S. L., Cochran, E. S., & Shearer, P. M. (2017). Source spectral
877 properties of small to moderate earthquakes in southern Kansas. *Journal of Geophysical*
878 *Research: Solid Earth*, 122, 8021-8034. doi:10.1002/2017JB014649
879 Trugman, D. T., & P. M. Shearer (2018). Strong Correlation between Stress Drop and Peak
880 Ground Acceleration for Recent M 1–4 Earthquakes in the San Francisco Bay Area, *Bulletin*
881 *of the Seismological Society of America*, 108, 2, 929-945. doi:10.1785/0120170245 .
882 Trugman, D. T., & Shearer, P. M. (2017a). Application of an improved spectral decomposition
883 method to examine earthquake source scaling in Southern California. *Journal of*
884 *Geophysical Research: Solid Earth*, 122, 2890–2910. doi:10.1002/2017JB013971
885 Trugman, D. T., & A. Savvaidis (2021). Source spectral properties of earthquakes in the
886 Delaware Basin of West Texas. *Seismological Research Letters*, 92 (4): 2477–2489. doi:
887 10.1785/0220200461.
888 Voyles, J. R., A. Pitarka, K. D. Koper, & M. M. Holt (2019). Simulated effects of shallow crustal
889 heterogeneity, surface topography, and seismic source depth on coda wave generation for
890 magnitude-based depth discrimination, Abstract S11E-0417 *presented at Fall Meeting of the*
891 *American Geophysical Union, Washington, DC, Dec. 9–13*.
892 Walter, W. R., S.-H. Yoo, K. Mayeda, & R. Gök (2017). Earthquake stress via event ratio levels:
893 Application to the 2011 and 2016 Oklahoma seismic sequences, *Geophysical Research*
894 *Letters*, 44, doi:10.1002/2016GL072348
895 Yoshimitsu, N., Ellsworth, W. L., & Beroza, G. C. (2019). Robust stress drop estimates of
896 potentially induced earthquakes in Oklahoma: Evaluation of empirical Green's function.
897 *Journal of Geophysical Research: Solid Earth*, 124, 5854– 5866.
898 https://doi.org/10.1029/2019JB017483
899 Zhang, J., X. Chen & R. E. Abercrombie (2019). Resolving the spatiotemporal variability of
900 small earthquake source parameters at Parkfield and their relationship with 2004 M6
901 Parkfield earthquake, Abstract S51E-0445 *presented at 2019 Fall Meeting, AGU, San*
902 *Francisco, CA, 9-13, Dec.*

903 Zoback, M. D., & Harjes, H.-P. (1997). Injection-induced earthquakes and crustal stress at 9 km
904 depth at the KTB deep drilling site, Germany. *Journal of Geophysical Research*, *102*(B8),
905 18477. https://doi.org/10.1029/96JB02814
906

907 **Table 1:** Information for the data sets used from the spectral decomposition studies. The velocity
908 structures are included in the Supporting Information. The GO-C and PO-P studies analysed both P and
909 S waves, but we use only the P-wave source spectra here for consistency. All are in California except
910 where noted.

| ID | Name | Reference | Number of events | $M_L$ range | $M_w$ range | Shallow and deep ranges[1] (km) | Low f for Mo: Hz (samples) | f range for fitting (Hz) | Velocity Model |
|---|---|---|---|---|---|---|---|---|---|
| Ha-H | Hayward Fault – on Hayward fault only | Hardebeck & Aron (2009) | 984 | 1-4.2 | 1.4-4.0 | <6 & 8-13 | 3.9-7.8 Hz (3-5) | 3.9-40[2] | Hardebeck & Aron (2009) – each side of fault |
| Li-T | Bay Area Livermore Basin[3] | Trugman & Shearer (2018) | 1622 | 1.5-4.2 | 1.9-3.9 | <6 & 10-24 | 2.5-4 Hz (5-7) | 2.5-25 | SF CVM[4] |
| SF-T | Bay Area SAF and HF[3] | Trugman & Shearer (2018) | 3037 | 1.5-4.3 | 1.7-3.9 | <5 & 8-22 | 2.5-4 Hz (5-7) | 2.5-25 | SF-CVM[4] |
| Pf-Z | Parkfield, San Andreas Fault | Zhang et al. (2019) | 4454 | 0-3 | 0.9-3.4 | <4.5 & 8-15 | 2-4 Hz (55-80) | 2-60 | Thurber *et al.* (2006) 1D approximations of each side of fault |
| Mo-R | Mogul, NV | Ruhl et al. (2020). | 4938 | 0-5.1 | 0.6-4.9 | <3 & 4.2-6.5 | 2.5-4 Hz (5-7) | 1.3-26 | Ruhl *et al.* (2016) |
| La-S | Landers cluster | Shearer *et al*. (2019) | 4729 | 0-4.4 | 0.3-4 | <5 & 10-26 | 2.5-4 Hz (5-7) | 1.3-25 | SCEC CVM-H15.1[5] |
| La-T | Landers aftershocks | Trugman & Shearer (2017) | 2673 | 1.1-4.3 | 1.7-4.1 | <3 & 6-15 | 2.5-4 Hz (5-7) | 2.5-25 | SCEC CVM-H15.1[5] |
| HM-T | Hector Mine aftershocks | Trugman & Shearer (2017) | 2128 | 1.1-4.4 | 1.8-4.0 | <3 & 4-18 | 2.5-4 Hz (5-7) | 2.5-25 | SCEC CVM-H15.1[5] |
| BB-T | Big Bear aftershocks | Trugman & Shearer (2017) | 2949 | 1.1-5 | 1.6-5 | <3 & 6-18 | 2.5-4 Hz (5-7) | 2.5-25 | SCEC CVM-H15.1[5] |
| SJ-T | San Jacinto Fault Trifurcation zone | Trugman & Shearer (2017) | 5591 | 1.1-5.4 | 1.5-5.4 | <7.5 & 10-21 | 2.5-4 Hz (5-7) | 2.5-25 | SCEC CVM-H15.1[5] |
| YD-T | Yuha Desert aftershocks | Trugman & Shearer (2017) | 7483 | 1.1-5.7 | 1.5-5.7 | <4 & 9-19 | 2.5-4 Hz (5-7) | 2.5-25 | SCEC CVM-H15.1[5] |
| Ri-T | Ridgecrest aftershocks | Trugman (2020) | 15671 | 1.3-5 | 1.4-4.4 | 0-3 & 7-14 | 2.5-4 Hz (6-9) | 3-30 | Lomax (2020) |
| Ka-T | Southern Kansas | Trugman *et al.* (2017) | 4040 | 1.1-5.2 | 1.7-5.2 | <4 & 6.5-11 | 2.5-4 Hz (5-7) | 2.5-25 | Rubinstein *et al*. (2018) |
| PO-P | Prague, OK | Pennington et al. (2021) | 1656 | -1-3.5 | 1.7-4.1 | <4.75 & 4.75-12 | 1-3 Hz (28-60) | 2-60 | Toth *et al.* (2012) |
| GO-C | Guthrie OK | Chen & Abercrombie (2020) | 850 | 1-4.3 | 1.9-4.3 | <6.6 & 6.9-26 | 2-2.25 Hz (64-67) | 2-40 | Chen (2016) |
| SS-C | Salton Sea Geothermal Field[3] | Chen & Shearer (2011) | 1693 | 0.3-5.1 | 1.8-3.8 | <4.5 & 6-8 | 3-5 Hz (6-8) | 3-14 | SCEC CVM-H15.1[5] and Chen & Shearer (2011) |
| BS-C | Salton Sea – Brawley seismic zone[3] | Chen & Shearer (2011) | 572 | 1-4.2 | 2-3.5 | <8.5 & 9-15 | 3-5 Hz (6-8) | 3-14 | SCEC CVM-H15.1[5] and Chen & Shearer (2011) |
| SG-G | San Gorgonio | Goebel *et al.* (2015) | 8010 | 0-4 | 1.5-4.3 | <8 & 13-24 | 1.6-3.1 Hz (3-5) | 2-20 | SCEC CVM-H15.1[5] |

[1] The maximum depth shown is the maximum depth used for all events in the analysis.

[2] Hardebeck & Aron (2009) used the frequency range 3.9-55 Hz, but we used a lower limit due to concerns about the low signal to noise ratio at high frequencies.

[3] Sub-area polygon in Table S11, Supporting Information.

[4] SCEC Community Model (Shaw *et al*., 2015; Small *et al.* 2017)

[5] SF-CVM regional 3D velocity model (Aagaard *et al*., 2020)

**Table 2:** Source parameters assumed to calculate the Synthetic Spectra shown in Figure 5. Values are calculated assuming the same travel time (10 s) for all events, and a corner frequency of 10 Hz for a shallow $M_W$2.5. These values are purely illustrative

| Case | $f_c$ (Hz) $M_W$3 (large) | | $f_c$ (Hz) $M_W$2 (small) | | $t^*$deep (s) | $t^*$shallow (s) |
|---|---|---|---|---|---|---|
| | Deep | shallow | Deep | Shallow | | |
| a: $Q$ increases with depth, Δσ constant | 5.6 | 5.6 | 17.8 | 17.8 | 0.0171 | 0.04 |
| b: $Q$ and Δσ increase with depth | 8.1 | 5.6 | 25.6 | 17.8 | 0.0171 | 0.04 |
| c: $Q$ constant, Δσ increases with depth | 8.1 | 5.6 | 25.6 | 17.8 | 0.04 | 0.04 |

## Figure Captions

**Figure 1:** Maps of the earthquakes used in the analysis. See Table 1 for details, and explanation of the legend IDs

**Figure 2:** Ratio of high to low frequency amplitude as a function of earthquake depth for Ridgecrest aftershocks. The event spectra are divided into 0.2 Mw unit bins on the basis of their relative moments. Each log-linear plot shows the ratio of the mean high frequency (15-20 Hz) to mean low frequency (2-5.5 Hz) amplitudes of each event spectrum as a function of hypocentral depth (green circles). The running mean of 50 samples is also shown (dark green circles). The two vertical dashed lines indicate the selected cut-off depths used to determine the "deep" and "shallow" earthquakes (Table 1). The pale orange lines are the 1D velocity structure (Lomax 2020, see Table 1). The spectra of deeper earthquakes have more high frequency energy, but this could represent either increasing stress drop with depth, or decrease in attenuation with depth.

**Figure 3:** Ratio of high to low frequency amplitude as a function of earthquake depth for all study regions, for the example magnitude bin Mw2.2-2.4. As in Figure 2, the dark green symbols are the running means, the vertical dashed lines indicate the depths used to select the "deep" and "shallow" earthquakes in each dataset, and the orange lines are the 1D velocity structure (see Table 1 for sources). The increase in high frequency energy with depth is observed to some degree in all data sets.

**Figure 4:** Cartoon Cross sections in which velocity and *Q* increase with depth, showing stations (black triangles), raypaths and groups of earthquakes (stars) considered. (a) Deep (dark red) and shallow (orange) larger events are corrected for attenuation using all smaller (EGF events, red), independent of depth. (b) Deep (dark blue) and shallow (pale blue) larger events are corrected for attenuation using deep (dark blue) and shallow (pale blue) EGF events, respectively. This color scheme is used throughout the paper (e.g., in Figures 5-9) for clarity.

952 **Figure 5:** Effects of increasing *Q* and stress drop ($\Delta\sigma$) with depth on synthetic spectra in 3
953 example cases. Top row: Brune spectra of large (M3.5, solid lines), shallow (pale blue) and
954 deep (dark blue) events and small (M2.5, dashed lines), shallow (pale blue) and deep (dark
955 blue) events (red is mean of small shallow and deep) for (a) constant $\Delta\sigma$, Q increasing with
956 depth, (b) Q and $\Delta\sigma$ increasing with depth, and (c) constant Q, $\Delta\sigma$ increasing with depth
957 (parameters in Table 2). Middle row: spectral ratios of deep large to deep small (dark blue),
958 shallow large to shallow small (pale blue), deep large to the mean of small (dark red) and
959 shallow large to the mean of small (orange). (d) constant $\Delta\sigma$, Q increasing with depth –
960 difference between event ratios disappears when depth-dependent correction included, (e)
961 Q and $\Delta\sigma$ increasing with depth – difference between event ratios decreases when depth-
962 dependent correction included, and (f) constant Q, $\Delta\sigma$ increasing with depth – depth
963 dependent correction has no effect. Bottom row: Comparison of spectral ratios with and
964 without depth dependent correction, (g) ratio of uncorrected deep / shallow ratios (red:
965 ratio of dark and pale red in d) compared to similar ratio for corrected ratios (blue: ratio of
966 dark and pale blue in e). Triangles show the mean values over the representative frequency
967 range 2-20 Hz. (h) and (i) show the same comparison for the other two example cases.

968 **Figure 6.** Spectral ratios of stacked large to small Ridgecrest aftershocks, to investigate the
969 effects of a depth dependent EGF correction. Compare to the synthetic example in Figure 5.
970 Each plot shows spectral ratios (solid lines) of the stacked large deep events to the stacked
971 small deep events (dark blue), the large shallow events to the small shallow events (pale
972 blue), the large deep events to all the small events (dark red) and the large shallow events
973 to all the small events (orange). The title of each plot indicates the minimum Mw of the
974 large and small events, both with a range of 0.2Mw. (a) is for a constant Mw difference
975 between large and small earthquakes, and (b) is for a constant-sized Mw for the small
976 earthquakes. The dashed lines are the fits of the Brune omega-squared spectral ratios to
977 the average data ratios. The corner frequency of the best fitting ratio is given on each plot,
978 with the number of larger events in the ratios in parentheses (D=deep, S=shallow, and
979 A=all). Thinner lines indicate less than 10 large or small events were included in the mean
980 ratios. The blue (depth-corrected) deep and shallow event spectral ratios are consistently

closer together than the red ratios that assume no dependence of attenuation with depth (compare to Figure 5d,e).

**Figure 7.** Depth differences in the event spectra: ratios of ratios – compare to Figure 5(g,h,i). Uncorrected for Depth (red): The large deep and shallow events are divided by the same selection of small events, and so the difference between the deep and shallow ratios is simply the ratio of the mean deep large event spectra to the mean shallow (each ratio is the mean for a different large Mw bin). Corrected for Depth (blue): In this case, for each large Mw bin, the blue curve represents the ratio of the (mean large deep spectra divided by the small deep spectra) to the (mean large shallow spectra divided by the small shallow spectra); again each ratio is for a large Mw bin. The similarity of the slope of the red curves in each region demonstrates that the difference in frequency content between shallow and deep events is independent of magnitude. The smaller slope of the blue curves shows that using the correct depth small EGF events can remove this depth-dependence to the frequency content, suggesting it is largely an attenuation effect.

**Figure 8:** Comparison of mean amplitude ratios of deep/shallow for each region – compare to Figure 5(g,h,i). The symbols indicate the mean values of the red and blue ratios shown in Figure 7, in the frequency range 2-20 Hz. Solid symbols represent ratios with at least 10 ratios, and open symbols those with at least 5; diamonds are for a constant different in magnitude between large and small, and circles are for a constant sized small event range. Note that the depth correction is able to remove much, and in some cases all, of the difference between the deep and shallow spectra. The interpoint variation between diamonds and circles, and between different magnitudes is indicative of the uncertainties.

**Figure 9.** Spectral ratio modeling results with and without correction for depth-dependent attenuation. The ratios of the calculated stress drop (proportional to corner frequency cubed, $fc^3$) of the deep to the shallow earthquakes are shown for each data set, with (blue) and without (red) a correction for depth-dependent attenuation, plotted against the minimum magnitude of the large earthquakes. For example, the Ridgecrest plot shows the ratios of the cubed corner frequencies for the different model fits in Figure 6. Solid symbols

represent ratios with at least 10 ratios, and open symbols those with at least 5; diamonds are for a constant different in magnitude between large and small, and circles are for a constant sized small event range. For most data sets, the depth corrections decrease the apparent difference in stress drop between the deep and small events, independent of the magnitude of the large or small events included.

**Figure 10.** Comparison of relative source parameters with difference in P-wave velocity. The ratios of corner frequencies between the deep and shallow earthquakes calculated using the approaches shown in Figures 9 and S7 are plotted against the ratio of the average P-wave velocity at the depths of the respective deep and shallow event populations included. Color is by data set, with alternating symbols to ease distinction. Multiple symbols per data set represent the different magnitude bins, and also the use of the alternative velocity models. (a) without correction for depth dependent attenuation and (b) with correction for depth dependent attenuation. The black dashed line represents a constant stress drop with depth, if rupture velocity is proportional to P-wave velocity.

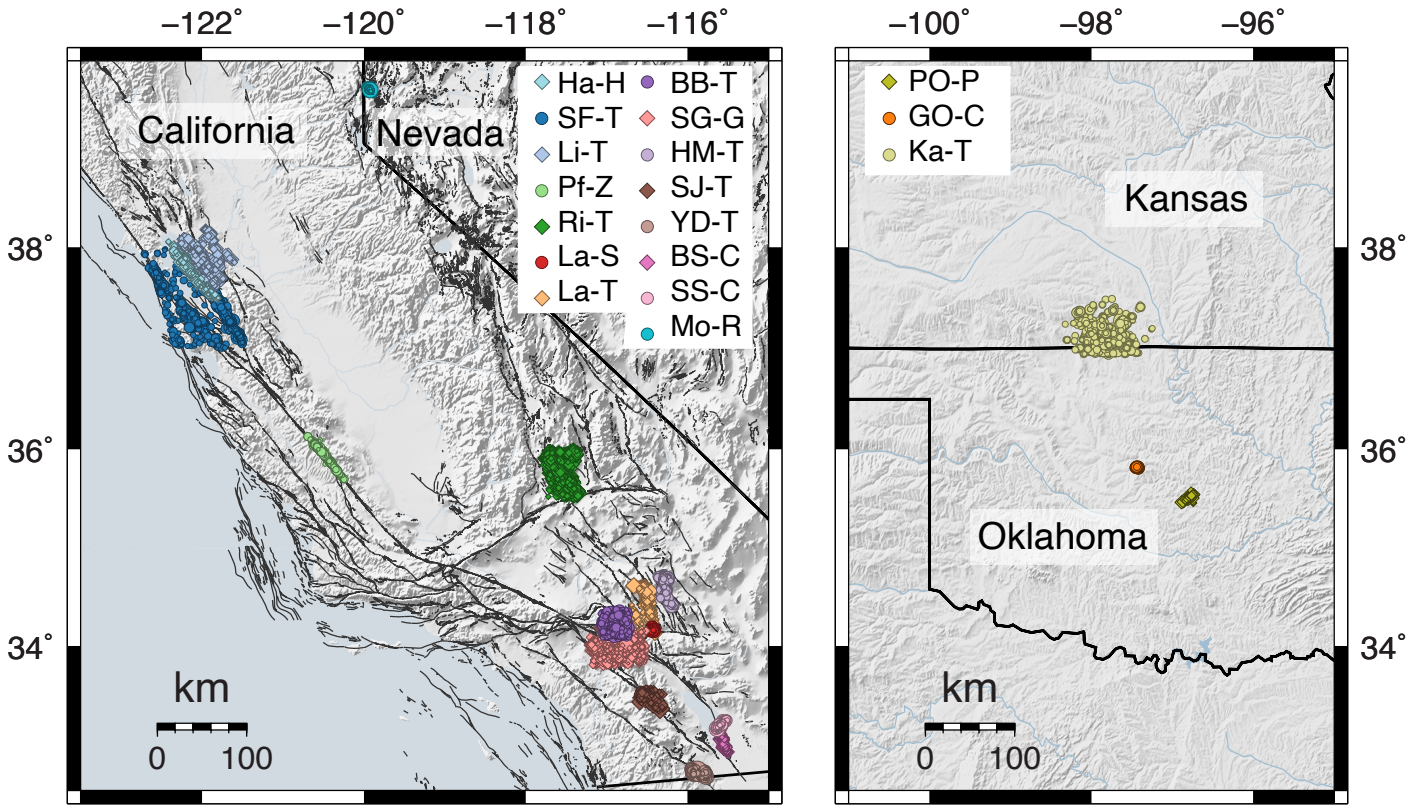


**Figure 1:** Maps of the earthquakes used in the analysis. See Table 1 for details, and explanation of the legend IDs.

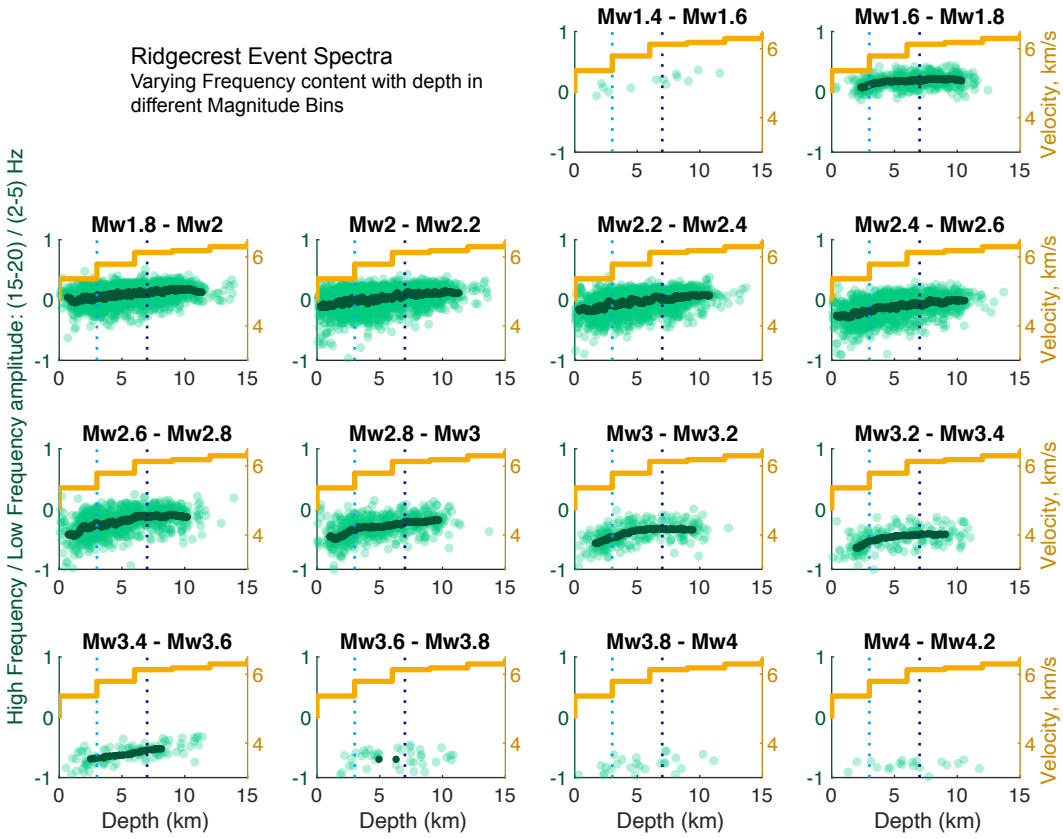


**Figure 2.** Ratio of high to low frequency amplitude as a function of earthquake depth for Ridgecrest aftershocks. The event spectra are divided into 0.2 Mw unit bins on the basis of their relative moments. Each log-linear plot shows the ratio of the mean high frequency (15-20 Hz) to mean low frequency (2-5.5 Hz) amplitudes of each event spectrum as a function of hypocentral depth (green circles). The running mean of 50 samples is also shown (dark green circles). The two vertical dashed lines indicate the selected cut-off depths used to determine the “deep” and “shallow” earthquakes (Table 1). The pale orange lines are the 1D velocity structure (Lomax 2020, see Table 1). The spectra of deeper earthquakes have more high frequency energy, but this could represent either increasing stress drop with depth, or decrease in attenuation with depth.

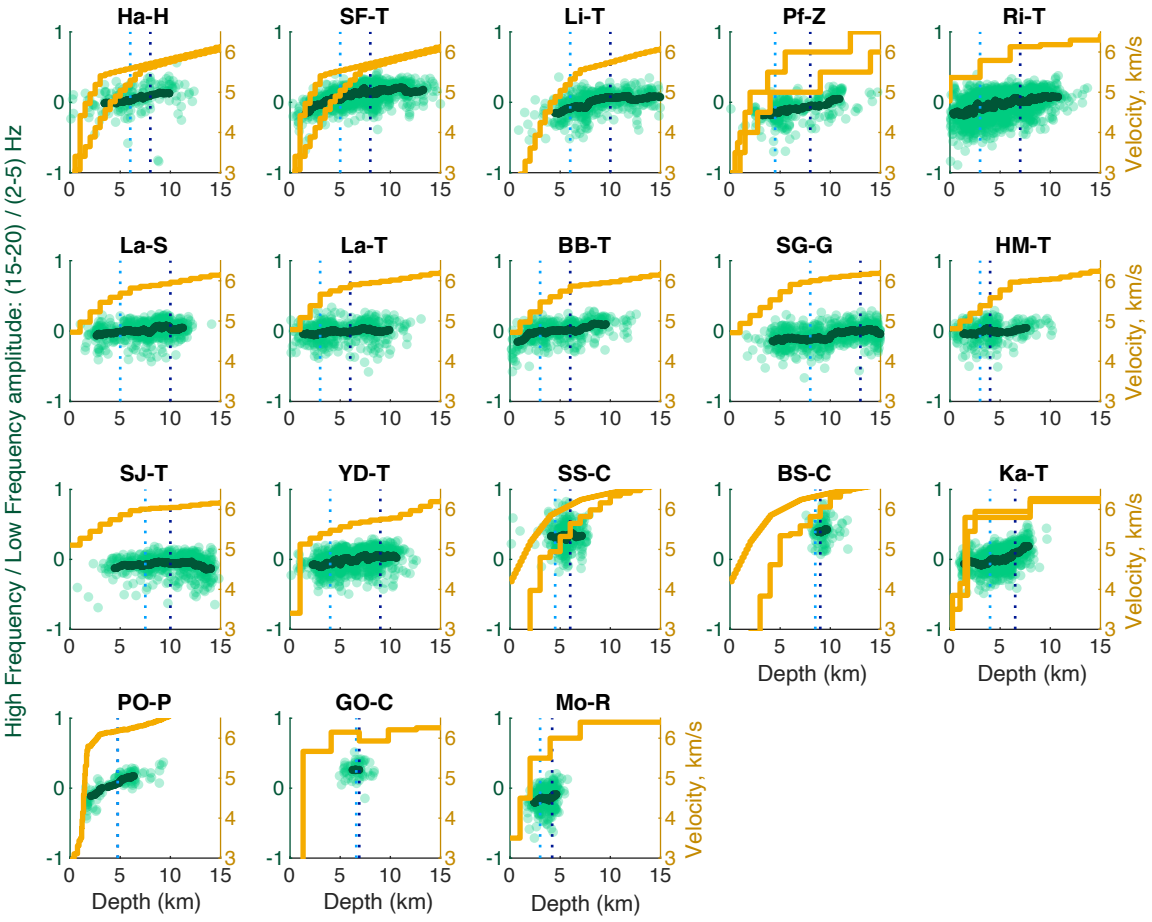


**Figure 3.** Ratio of high to low frequency amplitude as a function of earthquake depth for all study regions, for the example magnitude bin Mw2.2-2.4. As in Figure 2, the dark green symbols are the running means, the vertical dashed lines indicate the depths used to select the “deep” and “shallow” earthquakes in each dataset, and the orange lines are the 1D velocity structure (see Table 1 for sources). The increase in high frequency energy with depth is observed to some degree in all data sets.

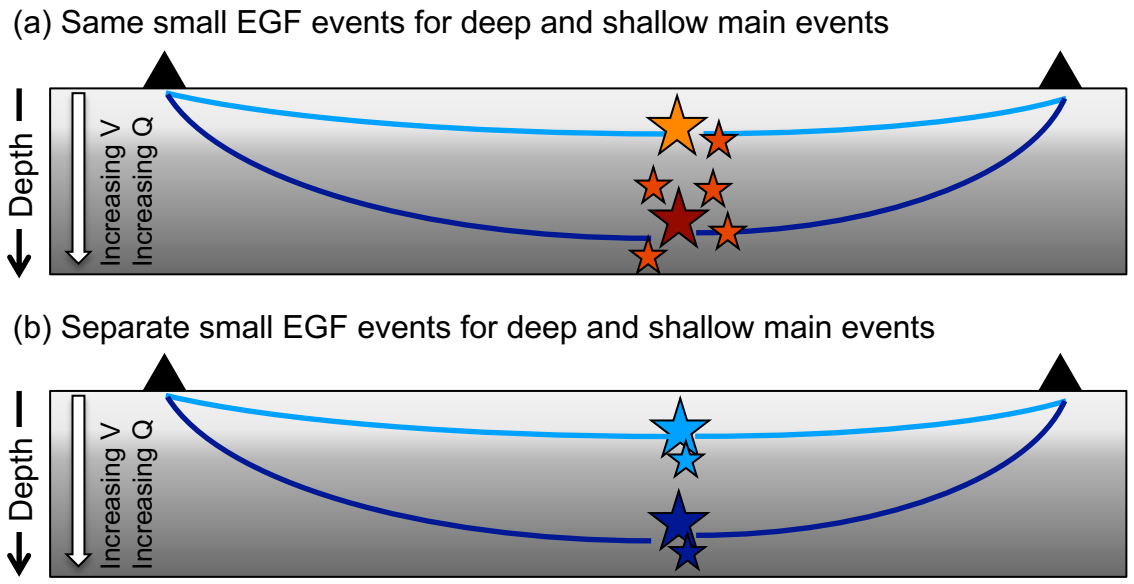


**Figure 4:** Cartoon cross sections in which velocity and *Q* increase with depth, showing stations (black triangles), raypaths and groups of earthquakes (stars) considered. (a) Deep (dark red) and shallow (orange) larger events are corrected for attenuation using all smaller (EGF events, red), independent of depth. (b) Deep (dark blue) and shallow (pale blue) larger events are corrected for attenuation using deep (dark blue) and shallow (pale blue) EGF events, respectively. This color scheme is used throughout the paper (e.g. in Figures 5-9) for clarity.

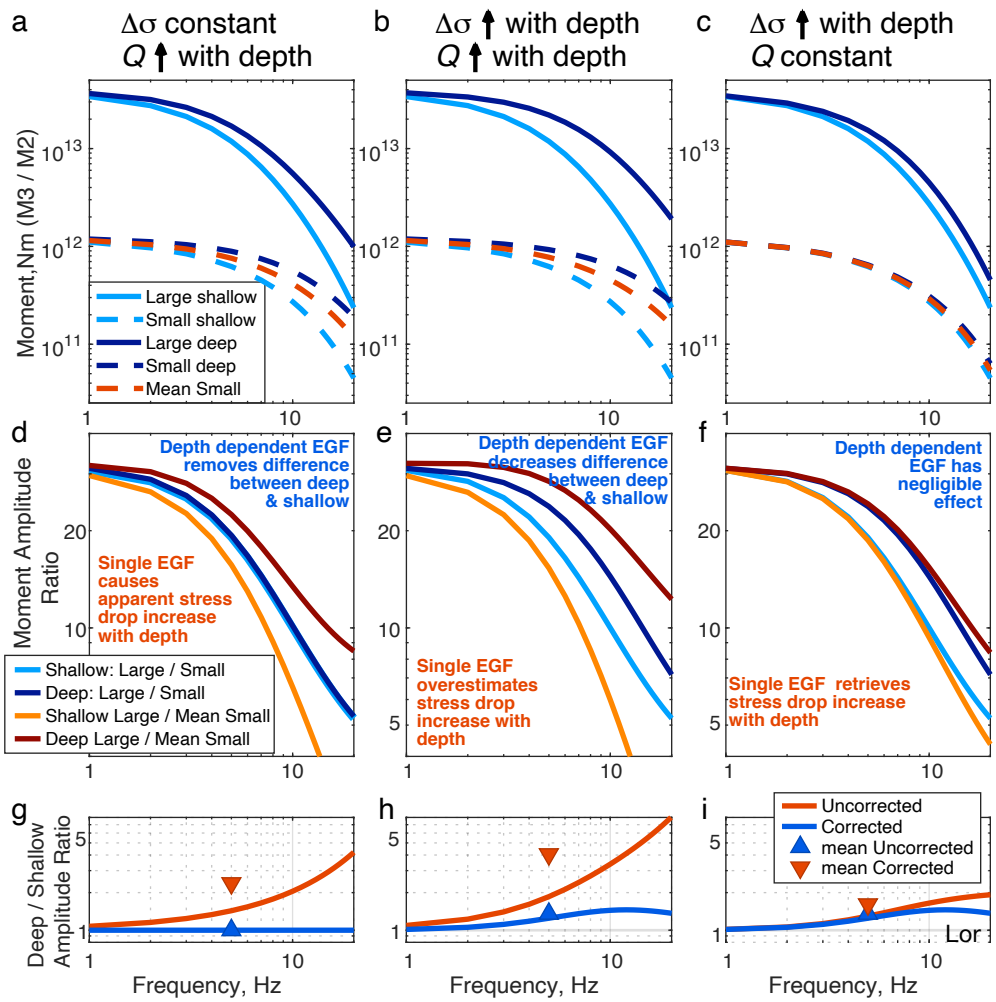


**Figure 5.** Effects of increasing *Q* and stress drop (Δσ) with depth on synthetic spectra in 3 example cases. Top row: Brune spectra of large (M3.5, solid lines), shallow (pale blue) and deep (dark blue) events and small (M2.5, dashed lines), shallow (pale blue) and deep (dark blue) events (red is mean of small shallow and deep) for (a) constant Δσ, *Q* increasing with depth, (b) *Q* and Δσ increasing with depth, and (c) constant *Q*, Δσ increasing with depth (parameters in Table 2). Middle row: spectral ratios of deep large to deep small (dark blue), shallow large to shallow small (pale blue), deep large to the mean of small (dark red) and shallow large to the mean of small (orange). (d) constant Δσ, *Q* increasing with depth – difference between event ratios disappears when depth-dependent correction included, (e) *Q* and Δσ increasing with depth – difference between event ratios decreases when depth-dependent correction included, and (f) constant *Q*, Δσ increasing with depth – depth dependent correction has no effect. Bottom row: Comparison of spectral ratios with and without depth dependent correction, (g) ratio of uncorrected deep / shallow ratios (red: ratio of dark and pale red in d) compared to similar ratio for corrected ratios (blue: ratio of dark and pale blue in e). Triangles show the mean values over the representative frequency range 2-20 Hz. (h) and (i) show the same comparison for the other two example cases.

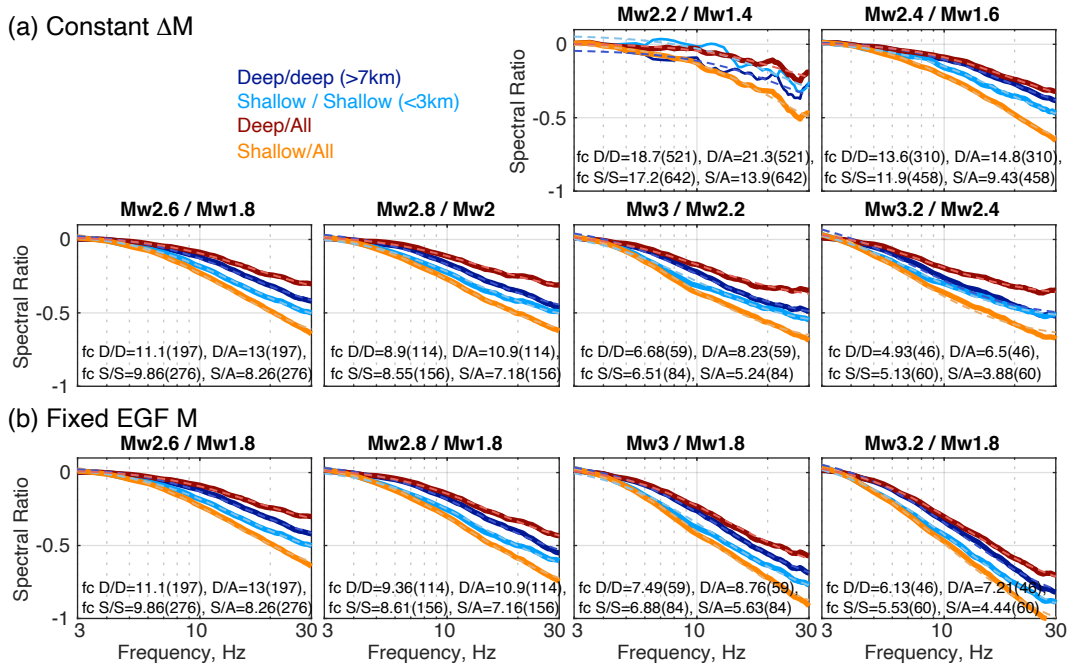


**Figure 6.** Spectral ratios of stacked large to small Ridgecrest aftershocks, to investigate the effects of a depth dependent EGF correction. Compare to the synthetic example in Figure 5. Each plot shows spectral ratios (solid lines) of the stacked large deep events to the stacked small deep events (dark blue), the large shallow events to the small shallow events (pale blue), the large deep events to all the small events (dark red) and the large shallow events to all the small events (orange). The title of each plot indicates the minimum Mw of the large and small events, both with a range of 0.2Mw. (a) is for a constant Mw difference between large and small earthquakes, and (b) is for a constant-sized Mw for the small earthquakes. The dashed lines are the fits of the Brune omega-squared spectral ratios to the average data ratios. The corner frequency of the best fitting ratio is given on each plot, with the number of larger events in the ratios in parentheses (D=deep, S=shallow, and A=all). Thinner lines indicate less than 10 large or small events were included in the mean ratios. The blue (depth-corrected) deep and shallow event spectral ratios are consistently closer together than the red ratios that assume no dependence of attenuation with depth (compare to Figure 5d,e).

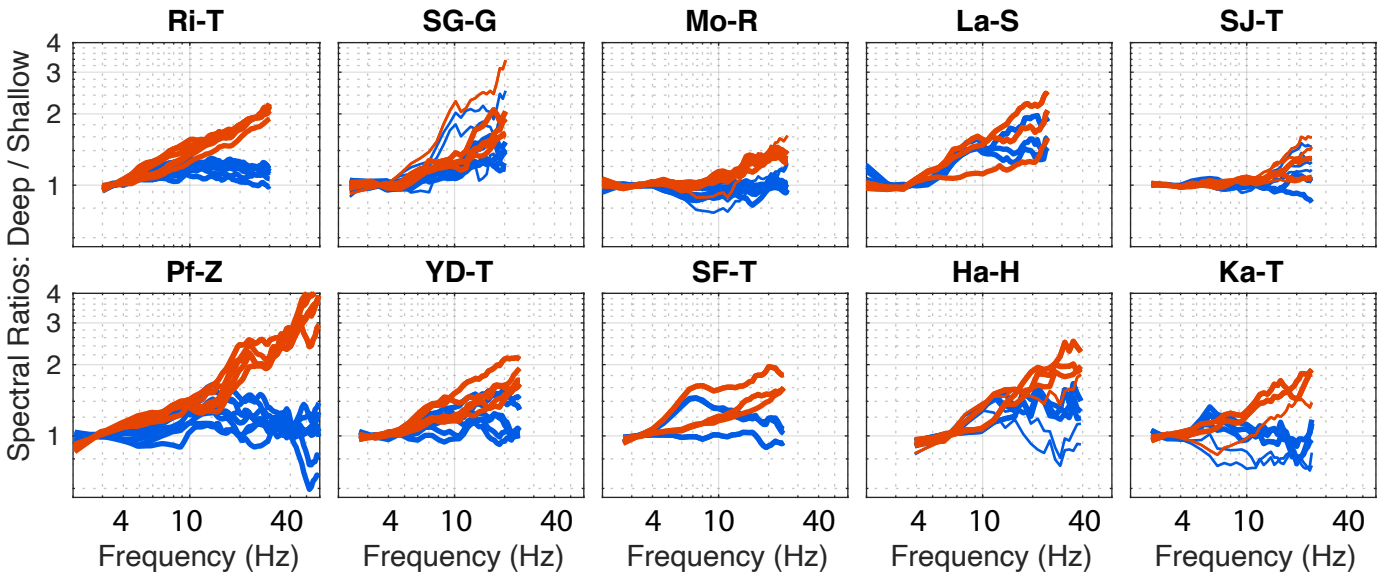


**Figure 7**. Depth differences in the event spectra: ratios of ratios – compare to Figure 5(g,h,i). Uncorrected for Depth (red): The large deep and shallow events are divided by the same selection of small events, and so the difference between the deep and shallow ratios is simply the ratio of the mean deep large event spectra to the mean shallow (each ratio is the mean for a different large Mw bin). Corrected for Depth (blue): In this case, for each large Mw bin, the blue curve represents the ratio of the (mean large deep spectra divided by the small deep spectra) to the (mean large shallow spectra divided by the small shallow spectra); again each ratio is for a large Mw bin. The similarity of the slope of the red curves in each region demonstrates that the difference in frequency content between shallow and deep events is independent of magnitude. The smaller slope of the blue curves shows that using the correct depth small EGF events can remove this depth-dependence to the frequency content, suggesting it is largely an attenuation effect.

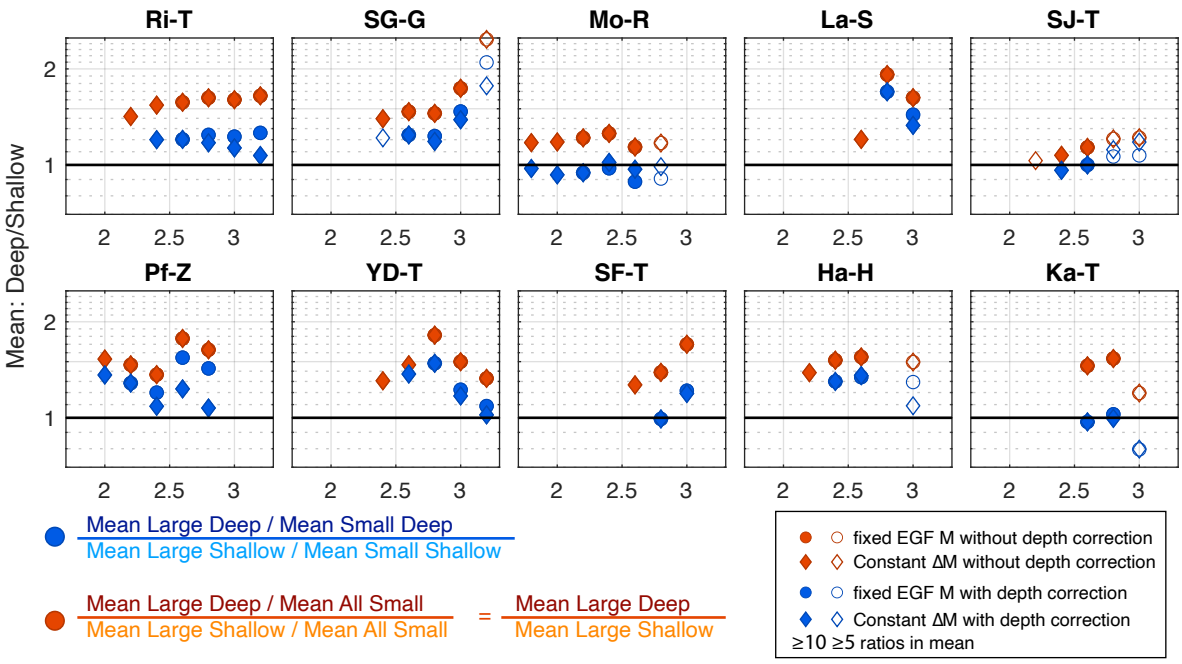


**Figure 8:** Comparison of mean amplitude ratios of deep/shallow for each region – compare to Figure 5(g,h,i). The symbols indicate the mean values of the red and blue ratios shown in Figure 7, in the frequency range 2-20 Hz. Solid symbols represent ratios with at least 10 ratios, and open symbols those with at least 5; diamonds are for a constant different in magnitude between large and small, and circles are for a constant sized small event range. Note that the depth correction is able to remove much, and in some cases all, of the difference between the deep and shallow spectra. The interpoint variation between diamonds and circles, and between different magnitudes is indicative of the uncertainties.

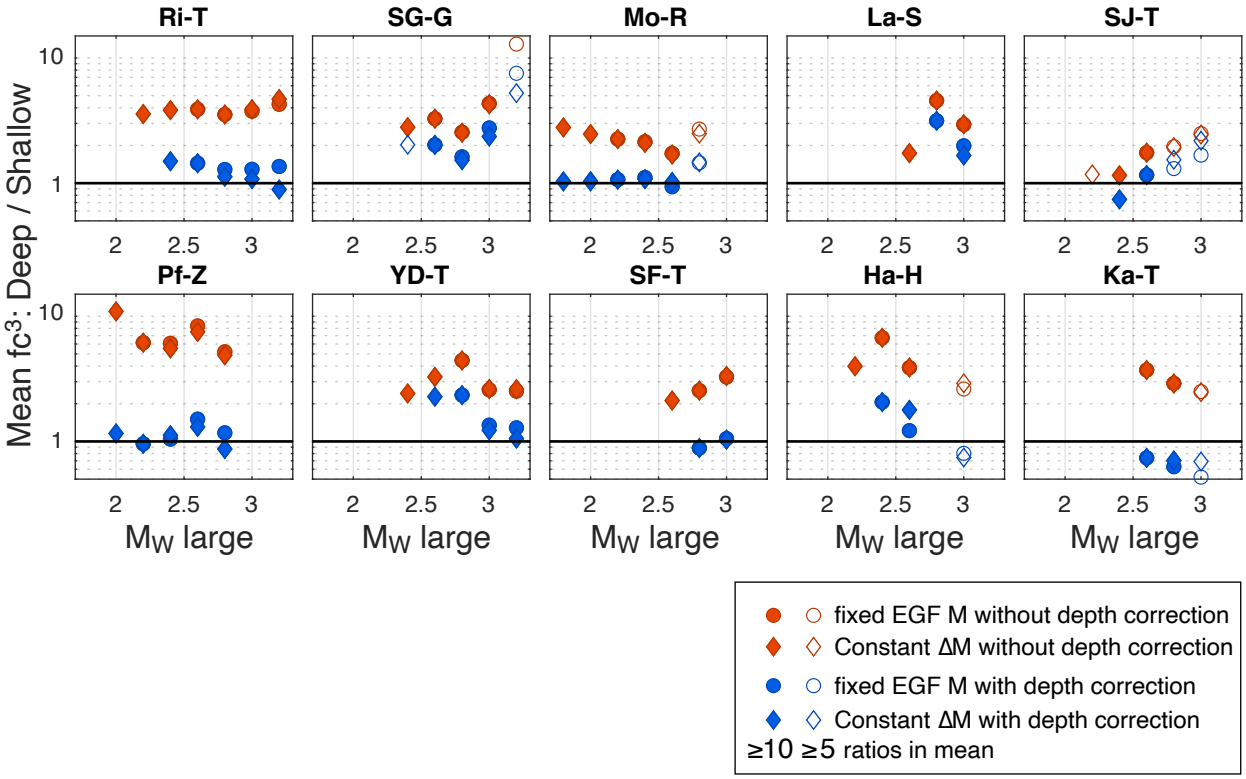


**Figure 9.** Spectral ratio modeling results with and without correction for depth-dependent attenuation. The ratios of the calculated stress drop (proportional to corner frequency cubed, $fc^3$) of the deep to the shallow earthquakes are shown for each data set, with (blue) and without (red) a correction for depth-dependent attenuation, plotted against the minimum magnitude of the large earthquakes. For example, the Ridgecrest plot shows the ratios of the cubed corner frequencies for the different model fits in Figure 6. Solid symbols represent ratios with at least 10 ratios, and open symbols those with at least 5; diamonds are for a constant different in magnitude between large and small, and circles are for a constant sized small event range. For most data sets, the depth corrections decrease the apparent difference in stress drop between the deep and small events, independent of the magnitude of the large or small events included.

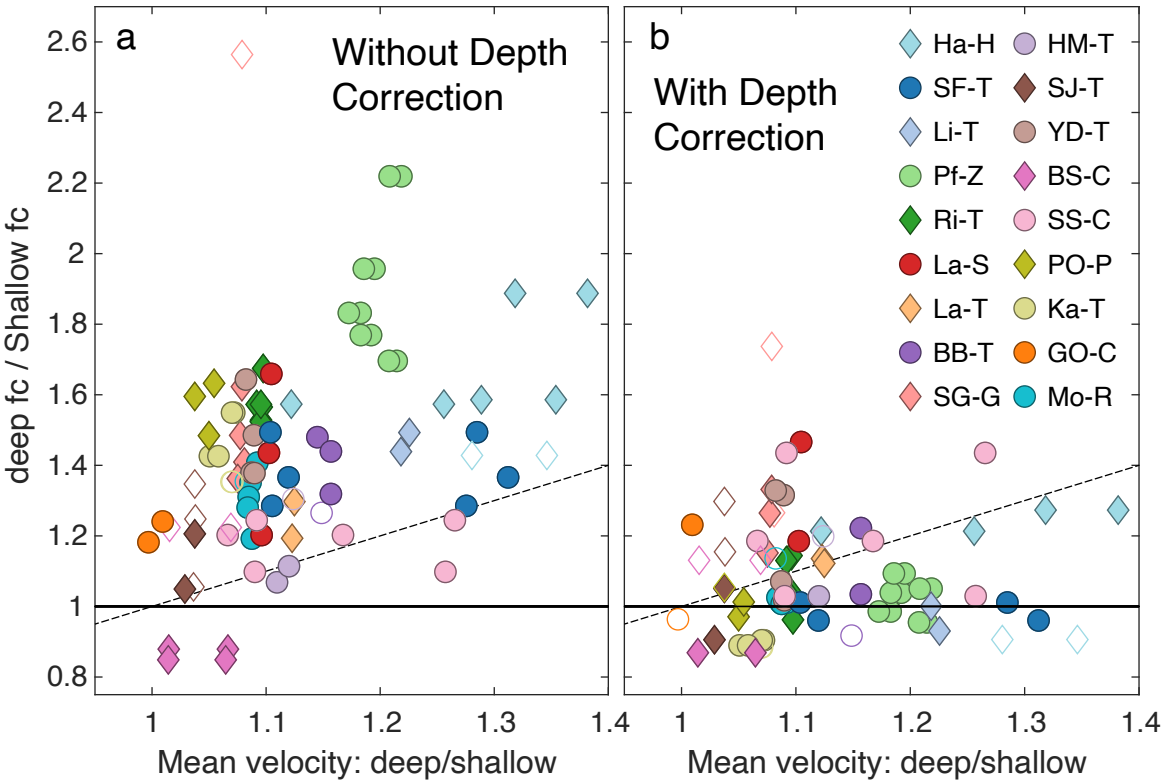


**Figure 10.** Comparison of relative source parameters with difference in P-wave velocity. The ratios of corner frequencies between the deep and shallow earthquakes calculated using the approaches shown in Figures 9 and S7 are plotted against the ratio of the average P-wave velocity at the depths of the respective deep and shallow event populations included. Color is by data set, with alternating symbols to ease distinction. Multiple symbols per data set represent the different magnitude bins, and also the use of the alternative velocity models. (a) without correction for depth dependent attenuation and (b) with correction for depth dependent attenuation. The black dashed line represents a constant stress drop with depth, if rupture velocity is proportional to P-wave velocity.